

國立交通大學

光電工程研究所

碩士論文

藉由氧化銦錫層之增強光學力於氮化矽波
導上進行微米粒子傳輸與分類



**Transport and sorting of micro-particles with enhanced
optical force on silicon nitride waveguide by ITO layer**

研究生：呂紹平

指導教授：李柏璵 博士

中華民國 一 百 年 八 月

藉由氧化銦錫層之增強光學力於氮化矽波導上進行微
米粒子傳輸與分類

**Transport and sorting of micro-particles with enhanced optical
force on silicon nitride waveguide by ITO layer**

研究生：呂紹平

Student : Shao-Ping Lu

指導教授：李柏聰 博士

Advisor : Dr. Po-Tsung Lee



A Thesis

Submitted to Department of Photonics
Institute of Electro-Optical Engineering
College of Electrical and computer Engineering
National Chiao Tung University

In partial Fulfillment of the Requirements
the Degree of
Master

In
Electro-Optical Engineering
August 2011

中華民國 一 百 年 八 月

藉由氧化銻錫層之增強光學力 於氮化矽波導上進行微米粒子傳輸與分 類

研究生：呂紹平 指導教授：李柏聰 博士

國立交通大學

光電工程研究所



這篇論文的目標為，在一個光容易耦合進入的波導結構上，增強消逝波與微米粒子的交互作用，以完成高效率且高穩定度的進場粒子傳輸系統。為此目的，我們研究光學作用力隨著實心波導幾何結構的改變。由模擬結果預測，較細薄的波導可以在較短波長處得到較強的推動力，而此推動力直接影響粒子的傳輸效率。為了達到多粒子的平行傳輸，我們必須同時考慮光穿透率與光學推進力；此穿透率為波導上傳遞光通過傳遞粒子後依然於波導上傳遞的比率。透過光穿透率與光學推進力的乘積，我們可以評定一波導結構進行多粒子平行傳輸的能力。為了進一步提升消逝波與粒子的交互作用，我們在波導結構及基板間加入 200 奈米厚之氧化銻錫層。模擬結果顯示，透過氧化銻錫層的金屬特性，光學作用力可有效的被增強。實驗結果顯示，以功率為一瓦特的光導入波導中，具有氧化銻錫層之 0.5 微米寬的波導可以以每秒 9.65 微米的速度傳輸直徑 2 微米的粒子，這結果是優於較寬的波導所呈現的，其速度更是比不具有氧化銻錫層之波導結構還快許多。此外，具有氧化銻錫層之波導也同時在側向以及垂直方向擁有較大的吸引光學力，可以有效率的捕捉粒子在波導之上的，達到穩定捕捉及傳遞。除此之外，我們也可以藉由與粒子尺寸的不同，所對應的光學力與速度的落差，來進行粒子分類的實驗。

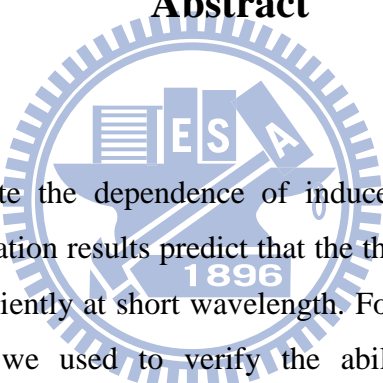
Transport and sorting of micro-particles with enhanced optical force on silicon nitride waveguide by ITO layer

Student : Shao-Ping Lu

Advisor : Dr. Po-Tsung Lee

Department of Photonics Institute of Electro-Optical Engineering
National Chiao Tung University

Abstract



In this thesis, we investigate the dependence of induced optical forces on geometry of solid-core waveguide. Simulation results predict that the thinner and narrower waveguide can transport particles more efficiently at short wavelength. For the parallel-transport system, the force-transmission product we used to verify the ability of particles manipulation of waveguides at the same time. We also find that an indium-tin-oxide (ITO) layer between the waveguide and substrate can further improve the optical forces. Experimental results show that when 1W power is coupled into waveguide, 0.5 μm wide waveguide with ITO layer underlaid can transport 2 μm particles for 9.65 $\mu\text{m/s}$, which is faster than that on the wider waveguides, and much faster than that on similar without ITO layer underlaid. The waveguide with ITO layer underlaid also have the greater attractive optical force in lateral and vertical direction, then it can trap particles efficiently at the equilibrium point above the waveguide. The particle-size dependent forces are used in the sorting experiments, and we can separate en-mass particles in practical system.

Acknowledgements

很感謝有兩年來學習以及歷練，對於研究所的所有一切、所見所聞都是在嘗試過後才會有所了解，在過程中，真的受到很多人的照顧，才能夠一一的過關斬將。首先要先感謝我的指導教授：李柏聰教授，提供完好的研究環境以及豐富的實驗室資源，並且在研究上適時的給予我寶貴的意見。

在這兩年以來研究中，非常感謝親自指導我的學長，林品佐學長，常常不厭其煩的在各方面教導我，無論在實驗或是研究上都給我很多建議以及實驗方向，過程中，也讓我看到自己有很多部分都需要再學習、努力的。在我在課業研究上遇到諸多問題，鼓勵我主動的去面對，找出問題的答案或是解決方法，真的是有好多說不出感激。

感謝本實驗室的學長，盧贊文、蔡家揚、郭光揚學長，總是給予我很多在實驗上或是生活上的幫助，以及共度實驗室生活上的一些瑣事，都是非常開心的；感謝陪伴我的實驗室的同學邱立勛、林雋歲、莊文齡、許書維、黃品睿，有了你們，在研究、運動、休閒、娛樂等等…讓實驗生活真的更加多采多姿；此外，還要感謝林佳欲、吳哲曉、蔡為智、劉權政、張開昊，雖然相處時間只有一年，不過跟你們在一起相處真的很棒。

最後，非常重要的，要感謝我的父母呂學禮先生以及黃彩雲小姐，感謝他們的養育之恩，從小到大都一直不段的給予我鼓勵以及意見，背後的支持，這份感恩，真的難以用言語來形容。感謝我的哥哥以及姊姊們，更是讓我無後顧之憂，能夠相互扶持成長，在此，更要特別感恩我所擁有的一切，人生中每一個示現，都是要要我懂得珍惜。特別感恩我生命中的導師，您給予、教導我的，真的太多太多了，我只能以永不放棄，以報師恩；感謝大家的支持與陪伴，讓我可以順利的邁向人生的下一階段，感恩有你們。

呂紹平 2011年8月

Table of Contents

Abstract (in Chinese).....	i
Abstract (in English)	ii
Acknowledgements.....	iii
Table of Content.....	iv
Figure Captions.....	vi
Table Captions.....	ix

Chapter 1. Introduction

1-1. Optical manipulation.....	1
1-1-1. Single laser beam manipulation.....	2
1-1-2. Near-field manipulation.....	4
1-1-2-1. Trapping and sensing.....	4
1-1-2-2. Transportation and sorting.....	7
1-2. Motivation.....	10

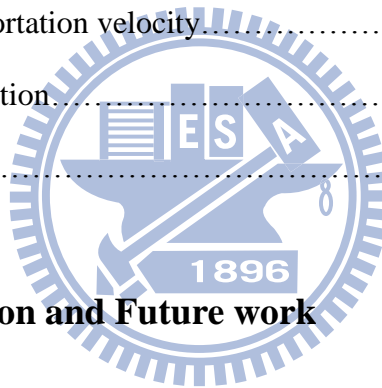
Chapter 2. Theoretical characterization and structure design

2-1. Theories.....	11
2-1-1. Optical force.....	11
2-1-2. Hydrodynamic analysis.....	14
2-2. Finite element method.....	16
2-3. Simulation results	18

2-3-1.	Waveguide geometry dependence of optical force.....	19
2-3-2.	Particle position dependence of optical forces.....	25
2-3-3.	Enhancement of optical forces by Indium Tin Oxide layer.....	30
2-4.	Summary.....	36

Chapter 3. Fabrication and measurement

3-1.	Fabrication	37
3-2.	Experimental setup.....	40
3-3.	Measurements.....	42
3-3-1.	Particle transportation velocity.....	42
3-3-2.	Sorting application.....	46
3-4.	Summary.....	47



Chapter 4. Conclusion and Future work

4-1.	Conclusion	48
4-2.	Future work.....	50

Reference	52
------------------------	-----------

Figure Captions

Fig. 1-1. Diagram showing the ray optics of a spherical Mie particle trapped in water by the highly focused light of a single-beam gradient force trap(Adapted from reference [5]).....3

Fig.1-2. Spatial distribution of (a) the light intensity (b) photon force exerted on the sphere near the aperture (adapted from reference [8]).....4

Fig.1-3. Field energy inside the bare cavity (solid line) and in the presence of a bead with diameter of $0.5a$ (dashed line). The inset shows the corresponding electric field distribution. (Adapted from reference [9]).....5

Fig.1-4. Experimental configuration for optically driving particles in a channeled waveguide. (Adapted from reference [10]).....7

Fig.1-5. The propulsion of $2\mu\text{m}$ glass particles and $1\mu\text{m}$ latex particles on $1\mu\text{m}$ silicon nitride waveguide. The sorting application can be used by the particle velocity different. (adapted from reference [12]).....8

Fig.1-6. (a) Schematic illustrating the nanoparticles transport in a slot waveguide. (b) Mode profile for a silicon-on-insulator 40-nm slot waveguide immersed in water (adapted from reference [13]).....9

Fig.2-1. The model (a) before (b) after mesh generation.....17

Fig.2-2. The schematic of modeling system. A particle near the waveguide would experience a combination of trapping and propulsion force.....18

Fig.2-3. Wavelength-dependent propulsion force F_x for these geometries.....20

Fig.2-4. The distribution of y component of electric field at $y=y_{\text{particle center}}$ for (a) $\lambda=1000\text{nm}$ (b) $\lambda=1500\text{nm}$ (c) $\lambda=2000\text{nm}$. Inset shows the streamline of power flow, respectively.....20

Fig.2-5. Diagram showing the ray optics of a spherical Mie particle trapped and propelled on the waveguide in water surrounding. The evanescent wave driven forces is separated by propulsion force and downward trapping force.....	21
Fig.2-6. The diagram shows the wavelength-dependent transmissions for these waveguides in the single trapped particle system.....	22
Fig.2-7. The products of propulsion force and transmission as functions of launching wavelength.....	23
Fig.2-8. Calculation of the downward trapping forces F_z on different width of waveguides for a wide range of wavelength with 300nm thickness.....	24
Fig.2-9. The diagram of cross-section of the system.....	25
Fig.2-10. Comparison of the downward trapping forces F_z on a particle with $2\mu\text{m}$ in diameter using different waveguides and launching wavelengths (1500 and 1550 nm) at varying vertical positions.....	26
Fig.2-11. Comparison of the propulsion forces F_x at varying vertical positions.....	27
Fig.2-12. The distribution of y component of electric field at $y=y_{\text{particle center}}$ for (a) $0.5\ \mu\text{m}$ (b) $1\ \mu\text{m}$ (c) $2\ \mu\text{m}$ wide waveguides.....	27
Fig.2-13. Comparison of the transverse trapping forces F_y on a particle with $2\ \mu\text{m}$ in diameter using different waveguide at $\lambda=1500$ and $\lambda=1550$ nm.....	28
Fig.2-14. Comparison of the Propulsion forces F_x using different waveguide at $\lambda=1500$ and $\lambda=1550$ nm.....	29
Fig.2-15. The cross-section of the system with the ITO layer.....	30
Fig.2-16. Comparison of guided power distributions on $0.5\ \mu\text{m}$ wide waveguide for (a) 300 nm (b) 200 nm (c) 100 nm (d) 30 nm (e) none thicknesses of ITO layer.....	31
Fig.2-17. The scheme of the electromagnetic field distribution of surface plasmon polariton at the interface between metal and dielectric materials.....	31
Fig.2-18. The dependence of ITO layer thickness propulsion force F_x for $0.5\ \mu\text{m}$ wide waveguide. (Operated at 1550nm).....	32

Fig.2-19. ITO layer enhanced downward trapping force F_z at varying vertical positions.....	33
Fig.2-20. ITO layer enhanced propulsion force F_x at varying vertical positions.....	33
Fig.2-21. ITO layer enhanced transverse trapping force F_y at varying transverse positions.....	34
Fig.2-22. Comparison of the forces for $0.5\mu\text{m}$ wide waveguide with ITO layer or not in three dimensions.....	35
Fig.3-1. The first part of fabrication process.....	37
Fig.3-2. The second part of fabrication process.....	38
Fig.3-3. The top- and tilted-view SEM pictures of these structures (a) $w=0.5\mu\text{m}$ (b) $w=1\mu\text{m}$ (c) $w=2\mu\text{m}$	38
Fig.3-4. The cross-section of entrance of $2\mu\text{m}$ wide waveguide.....	39
Fig.3-5. The diagram of the experimental setup.....	40
Fig.3-6. The experimental setup.....	41
Fig.3-7. Motion of $2\mu\text{m}$ particles (indicated by red arrows) as time evolves on (a) 0.5 , (b) 1 , and (c) $2\mu\text{m}$ wide waveguides in 1500nm waveguide. (d) (e) (f) shows the same system which under condition of 1550 nm in wavelength.....	42
Fig.3-8. Motion of $1\mu\text{m}$ particles (indicated by red arrows) as time evolves on (a) 0.5 , (b) 1 , and (c) $2\mu\text{m}$ wide waveguides in 1500nm waveguide. (d) (e) (f) shows the same system which under condition of 1550 nm in wavelength.	45
Fig.3-9. Motion of mix of $1\mu\text{m}$ and $2\mu\text{m}$ particles (indicated by red and blue arrows) as time evolves $1\mu\text{m}$ wide waveguides in 1500nm waveguide.....	46
Fig.4-1. Coupling principle between fiber and photonic wires by means of a grating.	50
Fig.4-2. (a) Passive optical sorting of micro-particles by using the suggested waveguide. (b) The particles will be guided and separated by the each waveguide which have different trapping abilities.....	51

Table Captions

Table.1-1. Calculation of the optical forces on different kinds of waveguides for glass spheres with 500 nm diameter (n=1.55) in water (n=1.33) (adapted from reference [11]).	8
Table.2-1. Simulation and geometric parameters.	19
Table.2-2. The characteristic trapping stiffness and decay length of the force profiles in Z-direction.	26
Table.2-3. The characteristic trapping stiffness of the force profiles in Y-axis.	28
Table.2-4. The characteristic trapping stiffness of the force profiles in Y-axis.	34
Table.2-5. The characteristic trapping stiffness and maximum forces of the force profile.	35
Table.3-1. The measured velocities of 2 μ m particles.	43
Table.3-2. Simulation and geometric parameters of taper fiber.	43
Table.3-3. The 2 μ m particle transport velocities when per watt power coupled into waveguides.	44
Table.3-4. The measured velocities of 1 μ m particles.	45

Chapter 1.

Introduction

1-1 Optical manipulation

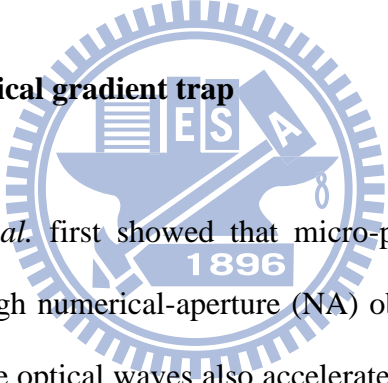
Base on the theory of photonics, light represented by wave-particle duality possess linear and angular momentum. In 1905, J.H. Poynting had deduced that when these momentums of light waves transfer to some objects, there will be forces and torques yielded to affect the motion of each object. Then he addressed about the radiation pressure, or called optical force, to the British Physical Society, “A very short experience in attempting to measure these forces is sufficient to make one realize their extreme minuteness—a minuteness which appears to put them beyond consideration in terrestrial affairs...” However, manipulating objects by light waves was not practical then, because the effects were not easy to be detected. On the other hand, there was no proper light source which can provide sufficient momentum change at that time. Hence the development of optical manipulation had come to a standstill, though it is an interesting topic.

Fortunately, C.H. Townes and A.L. Schawlow proposed the concept of laser in 1957 [1]. Later, T.H. Maiman made the first functioning ruby laser under pulse operation at 694 nm wavelength [2]. A powerful light source eventually realized until continuous-wave operation of laser was achieved [3], which ushered in a new era of optics. Many researches requiring highly coherent and collimated light waves with monochromatic property thus became achievable. Optical manipulation is one of them and started to progress rapidly.

In daily life, there are many tools such as tweezers or chopsticks we use to manipulate

macroscopic objects. However in biochemical applications, the objects to be manipulated, such as cells and tissues, are always easy to be damaged by any mechanical contact. Optical force with contactless and nondestructive properties thus becomes an ideal candidate for handling fragile objects. Furthermore, with reduced scale of objects, conventional mechanical tools have many limitations. For example, it is difficult for mechanical tools to trap tiny objects stably and precisely without any damage. But it does not limit the utility of optical force. Many works, as we introduce in the following sections, have shown that even nanometer sized particles can be trapped and manipulated stably and precisely by optical forces. Thus for researches in microscopic regime, optical force must be an indispensable tool, and we have to investigate it thoroughly.

1-1-1. A single beam optical gradient trap



In 1970, Ashkin *et al.* first showed that micro-particles can be trapped by using focused laser beams with high numerical-aperture (NA) objective lens to create high optical intensity at the focus [4]. The optical waves also accelerate the dielectric particles in the focal region and significantly affect the dynamics of micrometer sized neutral particles. Later, it was demonstrated that sphere could be levitated by balancing the force of radiation pressure against the force of gravity in water environment [5]. These experiments laid the groundwork for the rapid development of the field of optical trapping.

In the beginning, the behavior of transferred optical momentum was described by ray optics. Figure 1-1 illustrates the typical scattering model proposed by Ashkin, in which rays of a highly focused beam incident upon a dielectric sphere. Total force exerted on particle will be given by the total change in the momentum of the incident photons due to scattering, absorption, and spontaneous emission by the sphere.

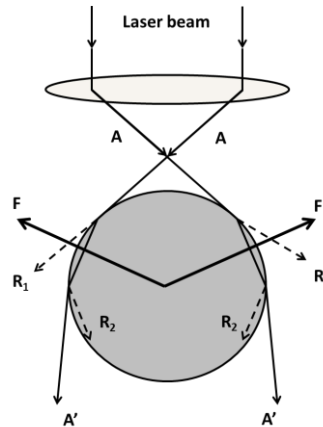


Fig. 1-1. Diagram showing the ray optics of a spherical Mie particle trapped in water by the highly focused light of a single-beam gradient force trap(Adapted from reference [5]).

In Fig. 1-1, the principal part of the momentum transfer from incident light to the particle is from rays A to A', which are refracted by the particle. Successive surface reflections, such as R₁ and R₂ contribute less momentum transfer. The momentum change of these waves result in the force F exerting on the particle. When particle is located out of the focal length, the incident waves and the total force are inverse. And thus the particle will be pulled toward the focal point. This is the main mechanism of optical trapping by using focused laser beam.

Over the years, focused laser beam had been widely utilized in many novel optical trapping and manipulation schemes. At that time, single beam gradient force optical trap, or called optical tweezers, was found to be the optimal configuration for trapping particles. Many works had shown that living biological cells can be trapped and manipulated by optical tweezers without optical damage. However, as the objects become smaller, spatial confinement of light must be more condensed. Finally, focusing system would meet the optical diffraction limit of propagation wave. Compared with sub-micrometer sized objects, such as protein, bacteria, and viruses, the focal spot is too large to trap such small particles precisely. Thus, optical tweezers becomes insufficient as the studied object becomes smaller.

On the other hand, focusing systems are always massive compared to the space particles are manipulated and the whole system is not portable. This may conflict with the purpose of developing integrated optical system. Therefore, the configuration of optical manipulation must be adapted for satisfying these requirements.

1-1-2. Near-field manipulation

In 1992, Kawata *et al.* demonstrated that evanescent field at the interface between two media can also affect the dynamics of objects in the near-field [6]. Since then, many researches about optical trapping and manipulation started to focus on the near-field configurations because of the following characters. The evanescent field is not limited by diffraction and can be tailored into sub-wavelength extend by structure design. Moreover, many structures utilizing evanescent field to manipulate particles can be easily integrated on the same chip. These characters just satisfy the mentioned requirements. By the function of manipulation, near-field configurations can be categorized into two types. One traps particle by the resonant enhanced evanescent field, and the other transports particle by the propagated evanescent field.

1-1-2-1. Trapping and sensing

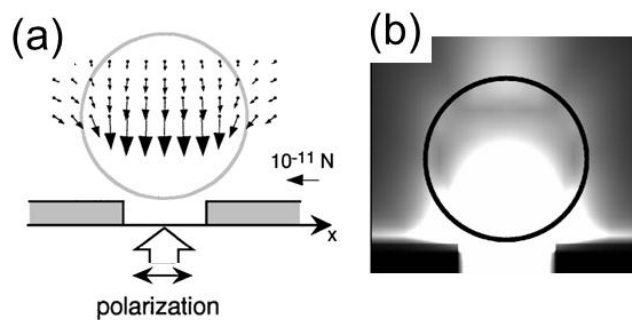


Fig.1-2. Spatial distribution of (a) the light intensity (b) photon force exerted on the sphere near the aperture (adapted from reference [8]).

After Kawata's work in 1992, many structures utilizing evanescent field to trap particles start emerging. In 1997, Novotny *et al.* used the evanescent field localized around metallic tip to trap particles of a few nanometers in size [7], in which the field is enhanced by surface plasma resonance. In 1999, Kawata *et al.* used plane wave impinging upon metallic nano-aperture to generate strong evanescent field in sub-wavelength extend for trapping sub-wavelength sized particles [8] which is shown in Fig.1-2. Later, the strong confinement of light by photonic crystal structure was utilized for optical trapping. Photonic crystal cavity consisted of hexagonal lattice in slab structure with single defect was first utilized. The resonant characteristic enhanced the evanescent field, and particles immersed in water with size in Rayleigh range are predicted to be stably trapped without easily disturbed by Brownian motion [9]. Moreover, an additional function to the optical trapping by using cavity structure is particle sensing. Particles with proper diameter trapped near photonic crystal cavities as shown in the inset of Fig.1-3 can shift the cavity out of resonance. By observing the shift of resonant peak in spectrum, we can recognize the size of particle. In other words, we would be able to trap and analyze the particle at the same time, and all of these are accomplished on a chip.

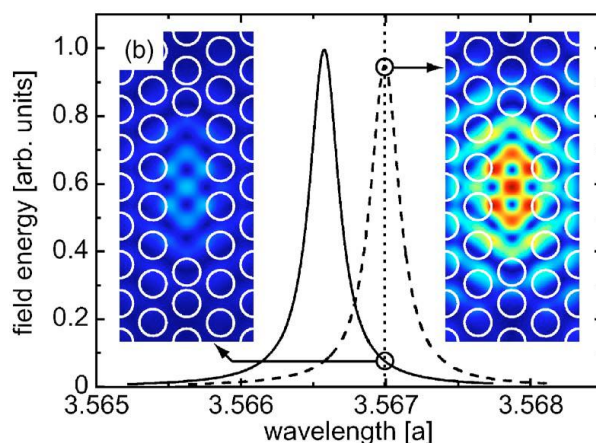


Fig.1-3. Field energy inside the bare cavity (solid line) and in the presence of a bead with diameter of $0.5a$ (dashed line). The inset shows the corresponding electric field distribution.

(Adapted from reference [9])

However for the purpose of developing lab-on-chip system, there must be some structures serve to transport particles between the integrated analyzing units on the chip. Micro-fluidic channels had been demonstrated to transport particles efficiently on the chip, but they require additional fluid pumping systems to make particles flow. To operate the chip all-optically, the particles must be transported by optical force. Based on these considerations, optical waveguide becomes the most suitable structure.



1-1-2-2. Transportation and sorting

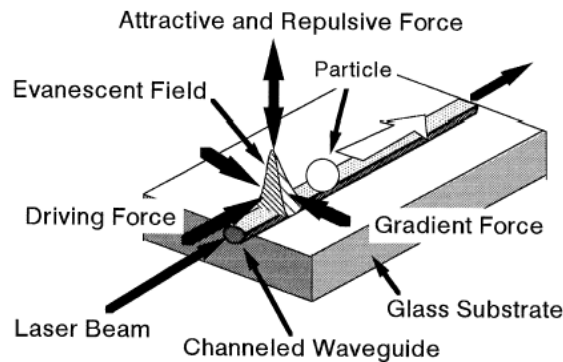


Fig.1-4. Experimental configuration for optically driving particles in a channeled waveguide.

(Adapted from reference [10])

In 1996, Kawata *et al.* first proposed transporting particles by the evanescent wave along a channel waveguide [10] which is shown in Fig.1-4. The evanescent field extending into the surrounding attracts particles toward the waveguide, and the propagation characteristic of the guided wave transport particles along the waveguide. Compared with the optical tweezers which traps and moves particles one by one, the optical waveguide can transport many particles simultaneously. And the transporting distance is not limited by the depth of focus as focusing systems are. Only the propagation loss dominates the distance particles can be transported. Until now, there have been many kinds of optical waveguide proposed and used for micro-propulsion in experiment. According to the refractive index contrast (Δn as compared to silicon oxide), these waveguides can be classified. Gaugiran *et al.* had compared the induced optical force on waveguides of different refractive indices under the same guided power in Table.1-1 [11]. They found that silicon nitride (Si_3N_4) waveguides with moderate refractive index contrast ($\Delta n = n_{\text{waveguide}} - n_{\text{SiO}_2} \sim 0.52$) can transport particles more efficiently than waveguides of lower refractive index contrast ($\Delta n \leq 0.04$) [12] can do. In this report, they also showed the feasibility of optical-sorting applications of micro-particles based on the different optical propulsion velocities corresponding to different

optical forces exerted upon the particles on a waveguide as shown in Fig.1-5.

	F propulsion	F gradient	Particle velocity
Potassium($\Delta n = 0.01$)	0.15 pN/W	-0.9 pN/W	10 $\mu\text{m/s/W}$
Cesium($\Delta n = 0.03$)	0.6 pN/W	-4 pN /W	41 $\mu\text{m/s/W}$
Nitride($\Delta n = 0.52$)	16.5 pN/W	-153 pN/W	1100 $\mu\text{m/s/W}$

Table.1-1. Calculation of the optical forces on different kinds of waveguides for glass spheres with 500 nm diameter ($n=1.55$) in water ($n=1.33$) (adapted from reference [11]).

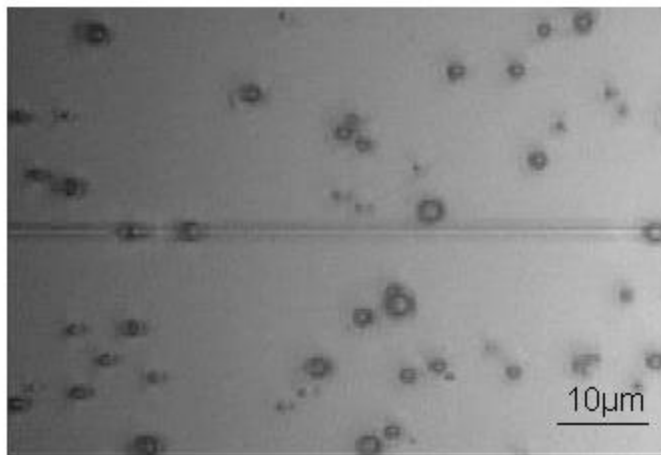


Fig.1-5. The propulsion of 2 μm glass particles and 1 μm latex particles on 1 μm silicon nitride waveguide. The sorting application can be used by the particle velocity different. (adapted from reference [12])

For waveguides of higher index contrast, the guided power would be well confined in the waveguide core with little portion extending into the surrounding. And the particles would experience only slight optical forces. That is why silicon waveguides on buried oxide layer are not utilized to transport particles. However, the trapped particles on these solid core waveguides only interact with the minority of the optical energy extended into surrounding in evanescent form. In order to solve this problem, Yang *et al.* used slot waveguide to transport

particles in the accessible low-index slot [13]. The slot waveguide structure is shown in Fig.1-6. The high index contrast in the slot region creates a pseudo transverse-electric mode that exhibits large electric field discontinuities at the slot-waveguide boundaries. The effect of the small slot size and the large field discontinuities at the high/low index boundaries generates a high-intensity eigenmode in the slot, such that the majority of the optical energy is confined within the accessible low-index region. And the particles would be able to interact with the majority of guided power. Although the slot waveguide can transport particles more efficiently, it is more difficult to couple light into a slot waveguide than into a solid-core waveguide if there is no any coupling structure designed at the waveguide entrance. Based on this consideration, how to enhance the optical forces for transporting particles along an easily coupled waveguide becomes an important issue.

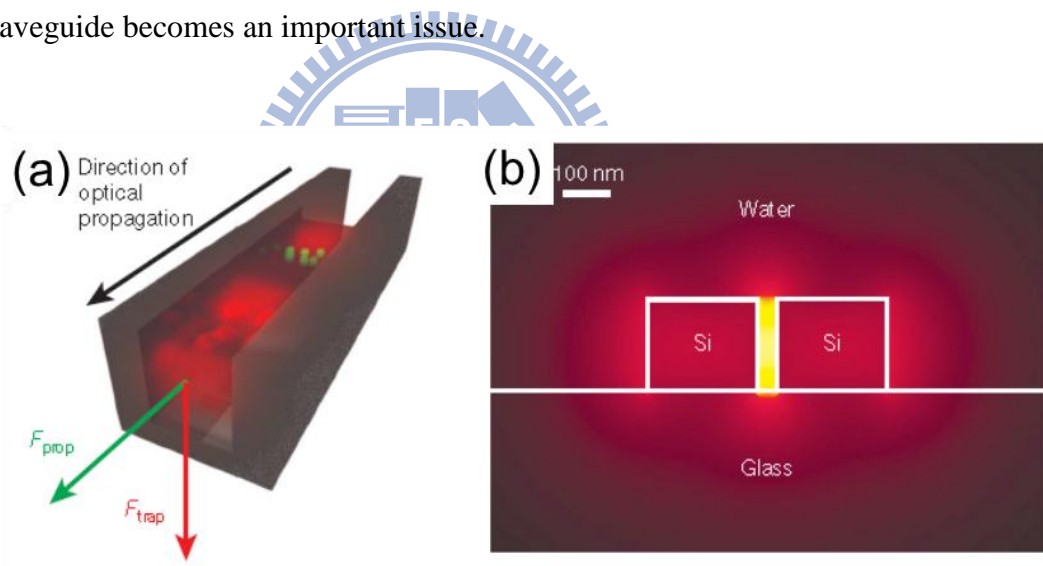


Fig.1-6. (a) Schematic illustrating the nanoparticles transport in a slot waveguide. (b) Mode profile for a silicon-on-insulator 40-nm slot waveguide immersed in water (adapted from reference [13])

1-2. Motivation

For developing lab-on-chip integration system, resonator-like optical cavities have shown their ability to trap nanometer-sized particles stably. By the resonant peak shift in spectrum, the trapped particle can also be identified and sensed. However, waveguide structures are indispensable for transporting particles between each functioning units on the chip. Although slot waveguide had shown its ability to transport particles more efficiently than solid core waveguides can do, it is more difficult to couple light into a slot waveguide than into a solid-core waveguide if there is no any coupling structure designed at the waveguide entrance. Based on this consideration, how to enhance the optical forces for transporting particles along an easily coupled waveguide becomes an important issue. Researchers had shown that using silicon nitride waveguide, with moderate refractive index contrast Δn , to transport particles is more efficiently than using waveguides of lower Δn . In this thesis, we investigate the dependence of optical force on the geometry of silicon nitride waveguide for yielding higher optical forces for transporting micro-particles. To our best knowledge, this investigation had not been done. For further enhancing the optical forces, we introduce an indium tin oxide (ITO) layer between the waveguide and the substrate. The conductor-like property of ITO layer forces the evanescent field to extend upward deeper into the water surrounding and interact stronger with the particles.

Chapter 2.

Theoretical characterization and structure design

2-1. Theories

2-1-1. Optical force

In order to understand the behavior of particles around the waveguide, it is necessary to calculate the optical force acting on a particle. Assumptions and numerical analysis are used according to the particle size. For particles with diameter much larger than the wavelength of scattered light, the optical forces acting on a spherical particle were presented by Barton et al [14]. Mie's scattering theory [15] and ray optics [16] have been employed as simple and excellent approximations that suffice for describing the behavior of the system.

As the particle have a radius α which is much smaller than the wavelength of the scattered light ($\alpha \ll \lambda/20$), which is so called the Rayleigh particle, can be considered as with an induced dipole moment density $\vec{P}(\vec{r}, t)$. Therefore, the electromagnetic force density can be described as the following equation:

$$\vec{f}(\vec{r}, t) = (\vec{P}(\vec{r}, t) \cdot \nabla) \vec{E}_m(\vec{r}, t) + \frac{\partial \vec{P}(\vec{r}, t)}{\partial t} \times \vec{B}_m(\vec{r}, t) \quad (2.1)$$

where \vec{E}_m is the electric field, \vec{B}_m is the magnetic flux field in a homogeneous medium.

The dipole moment density is the polarization of the particle (in units of As/m²): $\vec{P}(\vec{r}, t) = \alpha$

$\varepsilon_m \vec{E}_m(\vec{r}, t)$, is assumed to be proportional to the incident field \mathbf{E}_m and the polarizability α .

The permittivity in the medium is $\varepsilon_m = n_m^2 \varepsilon_0$. Using the vector identity and Maxwell equation, we can rewrite Eq. (2.1) as

$$\vec{f}(\vec{r}, t) = \alpha \varepsilon_m \frac{\nabla |\vec{E}_m(\vec{r}, t)|^2}{2} + \alpha \varepsilon_m \frac{\partial}{\partial t} [\vec{E}_m(\vec{r}, t) \times \vec{B}_m(\vec{r}, t)] \quad (2.2)$$

The vector product of the magnetic and the electric field is proportional to the Poynting vector, the time-average modulus of the Poynting vector is the intensity $I(\mathbf{r})$, which describes the number of photons per time and area in units of volt-amperes per square meter:

$$\bar{I}(\vec{r}) = \left\langle |\vec{S}(\vec{r}, t)| \right\rangle_T = n_m \varepsilon_0 c / 2 |\vec{E}_m(\vec{r})|^2 \quad (2.3)$$

Photons carry this energy as well as a momentum \mathbf{m} per volume at velocity c/n_m . The momentum density (Abraham's form) given in units of nanoseconds per cubic meter is

$$\vec{m}(\vec{r}, t) = \vec{S}(\vec{r}, t) / c^2 = \varepsilon_m / n_m [\vec{E}_m(\vec{r}, t) \times \vec{B}_m(\vec{r}, t)] \quad (2.4)$$

Averaging the force density $\vec{f}(\vec{r}) = \left\langle \vec{f}(\vec{r}, t) \right\rangle_T$ over one temporal period $T=1/\omega$ and using Eqs. (2.4) and (2.5), we can write Eq. (2.3) in the form

$$\vec{f}(\vec{r}, t) = \frac{\alpha n_m}{2c} \nabla I_m(\vec{r}) + \alpha n_m \frac{\Delta m_m(\vec{r})}{\Delta t} = \vec{f}_{grad}(\vec{r}) + \vec{f}_{scat}(\vec{r}) \quad (2.5)$$

In free-space, the optical forces on a small particle are often approximated by a

gradient force and a scattering force due to a strong field distribution near the focal point of a beam. However, these approximations fail to describe the forces when the particles and the waveguides are similar in dimension to the wavelength of the light used, and particles would experience significant distribution of evanescent fields. In this case, Maxwell stress tensor was a rigorous approach for calculating the optical forces.

The gradient and the scattering forces on a particle can be described as an electromagnetic stress using the Maxwell stress tensor:

$$\vec{T}_M = DE + HB - \frac{1}{2}(\vec{D} \cdot \vec{E} + \vec{H} \cdot \vec{B})I \quad (2.6)$$

where T_M represents the Maxwell stress tensor, E is the electric field, B is the magnetic flux density, D is the electric displacement, H is the magnetic field, and I is the isotropic tensor. Since we are interested in the transport processes which are much longer than the optical period on time scale, we use the time-averaged Maxwell stress tensor:

$$\langle T_M \rangle = \left\langle DE + HB - \frac{1}{2}(D \cdot E + H \cdot B)I \right\rangle \quad (2.7)$$

when expanded out, the equation becomes

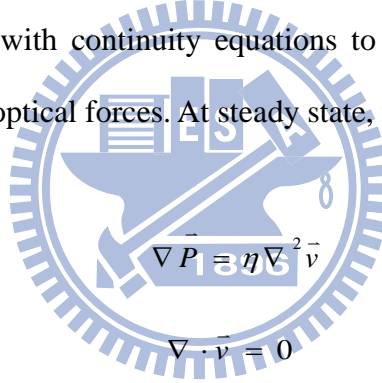
$$T_M = \begin{pmatrix} D_x E_x + B_x H_x & D_x E_y + B_x H_y & D_x E_z + B_x H_z \\ -\frac{1}{2}(D \cdot E + B \cdot H) & D_y E_y + B_y H_y & D_y E_z + B_y H_z \\ D_y E_x + B_y H_x & -\frac{1}{2}(D \cdot E + B \cdot H) & D_z E_z + B_z H_z \\ D_z E_x + B_z H_x & D_z E_y + B_z H_y & -\frac{1}{2}(D \cdot E + B \cdot H) \end{pmatrix} \quad (2.8)$$

where the subscripts x, y, and z signify the coordinate directions. By integrating the time-averaged Maxwell stress tensor on the surface enclosing the particle, we can determine the total electromagnetic, F_{EM} , force acting on the system by

$$\vec{F}_{EM} = \oint_S (\langle \vec{T}_M \rangle \cdot \vec{n}) dS \quad (2.9)$$

2-1-1-2. Hydrodynamic analysis

Since the optical forces acting on particles are independent of the hydrodynamic properties of the fluid, the problems of optical and hydrodynamics can be decoupled. Here we use Navier-Stokes's theory with continuity equations to describe the motion of particle in fluid under the influence of optical forces. At steady state, these equations are



$$\nabla P = \eta \nabla^2 \vec{v} \quad (2.10)$$

$$\nabla \cdot \vec{v} = 0 \quad (2.11)$$

where \vec{v} is the flowing velocity of fluid, η is viscosity of the fluid, and \vec{P} is the pressure in the system. Under these conditions the flow stress tensor \vec{T}_F is given by

$$\vec{T}_F = -PI + \eta (\nabla v + \nabla v^T) \quad (2.12)$$

where I is the identity tensor, The hydrodynamic drag force F_D on the particle resulting from fluid flow is described by

$$\vec{F}_D = \oint_S (\vec{T}_F \cdot \vec{n}) dS \quad (2.13)$$

where \vec{n} is surface normal vector.

Generally, hydrodynamic drag force is opposite to the optical force in direction. Optical force balanced by fluidic drag force makes particle move with a constant speed, which is called terminal speed and is linearly proportional to the optical force. We use Navier-Stokes law to find the terminal velocity V_t for a particle of radius a . For the simplest case, the particle is assumed to move through an infinite quiescent fluid. The hydrodynamic drag force F_D is described by

$$F_D = 6\pi\eta aV_t \quad (2.14)$$

where a is the particle radius, η is viscosity of the fluid, which in our case is water ($\eta_{\text{water}}=10^{-3}\text{Pa s}$). In the case of a particle near a waveguide surface we make use of the following modified expression.

$$F_D = 6\pi\eta aCV_t \quad (2.15)$$

where C is a constant that contains the relationship between hydrodynamic drag force and the velocity. Fixen's Law gives the constant term as,

$$C = \frac{1}{\left[1 - \frac{9}{16} \left(\frac{a}{h} \right) + \frac{1}{8} \left(\frac{a}{h} \right)^3 - \frac{45}{256} \left(\frac{a}{h} \right)^4 - \frac{1}{16} \left(\frac{a}{h} \right)^5 \right]} \quad (2.16)$$

where h is the distance between the center of the particle and the surface.

2-2. Finite element method

The finite element method (FEM) is a numerical technique for finding solutions of partial differential equations (PDE). For complicated optical systems, it can solve the boundary value problem, eigenvalue problem and find the steady state solution of a system by employing variational method. To apply this method, it requires discretizing a continuous domain into a set of discrete sub-domains, usually called elements, and the solution of each element would be approximated by certain characteristic form to solve the problems.

Here, the wave equations in the frequency domain for the magnetic and the electric fields are

$$\nabla \times (\varepsilon^{-1}(\vec{r}) \nabla \times \vec{H}(\vec{r})) = \frac{\omega^2}{c^2} \vec{H}(\vec{r}) \quad (2.17)$$

$$\varepsilon^{-1}(\vec{r}) \nabla \times \nabla \times \vec{E}(\vec{r}) = \frac{\omega^2}{c^2} \vec{E}(\vec{r}) \quad (2.18)$$

where c is the vacuum speed of light. To solve the wave equation for either magnetic or the electric field in frequency domain together with boundary conditions, standard FEM method proceeds in three steps. First, the wave equations are identified as solutions of certain variational problems where boundary conditions at the surface ∂V have been incorporated as additional terms of lagrangian L . The most general variational formulation for the electric field is given by

$$L(\vec{E}) = \frac{1}{2} \int_V dr^3 \left[\frac{1}{\mu} (\nabla \times \vec{E}) \cdot (\nabla \times \vec{E}) - \frac{\omega^2}{c^2} \varepsilon \vec{E} \cdot \vec{E} \right] + \int_{\partial V} d\vec{S} \left[\frac{\gamma_e}{2} (\vec{n} \times \vec{E}) \cdot (\vec{n} \times \vec{E}) - \vec{E} \cdot \vec{U} \right] + i \frac{\omega}{c} \sqrt{\frac{\mu_0}{\varepsilon_0}} \int_V dr^3 \vec{E} \cdot \vec{j} \quad (2.19)$$

where μ is the magnetic permeability and ε is dielectric function both may varied in space. In addition, \vec{n} denotes the outward normal at the surface ∂V and the electric field has to

satisfy the Dirichlet boundary condition $\vec{n} \times \vec{E} = 0$ on ∂S . γ_e and \vec{U} are known quantities which are used to represent various other types of boundary conditions such as impedance boundary conditions and Sommerfeld radiation conditions. Finally, radiation sources within the computational domain V are described through the spatially varying current density \vec{j} .

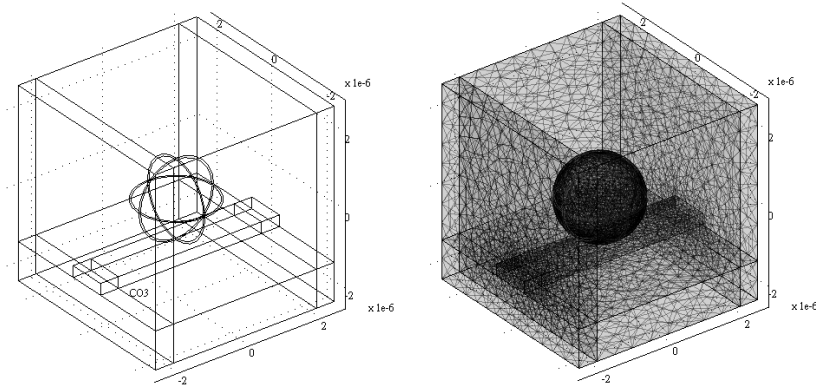


Fig.2-1. The model (a) before (b) after mesh generation.

The second step is the most demanding step which consists of the discretization of the Lagrangian. The computational domain V is divided into a number of small-volume elements, the so-called finite elements. Within each element, the electric field is expanded into a series of certain elementary functions with unknown coefficients. It becomes possible to approximately enforce the div-conditions of the electric field within a given element as long as the dielectric function does not vary within this element. Fig.2-1 shows the model with/without mesh generation in someone case.

In the final step, these expansions facilitate the transformation of the variational eqs. 2.19 into a sparse set of linear equations via the Galerkin method. This matrix system can subsequently be solved via advanced linear algebra methods, either for obtaining eigenfrequencies and eigenmodes of the system of interest or to determine scattering cross sections of complex structures as well as transmittance and reflectance through functional elements.

2-3. Simulation results

Fig.2-2 illustrates the model system and computational domain used in this study. The model represents a silicon nitride waveguide which is on glass substrate and clad in water environment. As the evanescent mode from this hybrid system appeared, the suspend particles will be attracted by the extended field in the water medium, and thus the particle can access the mode and interact with the waveguide. Generally, the optical force can be divided into trapping and propulsion forces, which attracts and propels the particle, respectively.

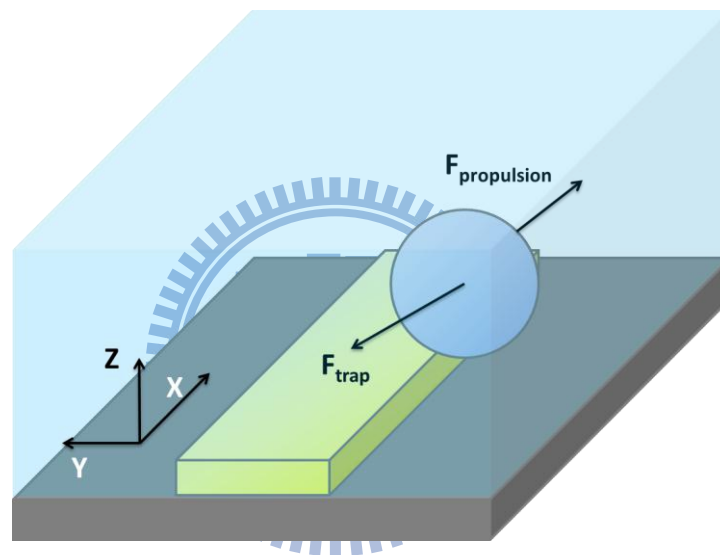


Fig.2-2. The schematic of modeling system. A particle near the waveguide would experience a combination of trapping and propulsion force.

To characterize the trapping situation as well as the maximum trapping force in all three dimensions in our system, we used the commercial software package (COMSOL) to carry out the detailed three-dimensional finite element numerical analysis. The material properties of the waveguide structures, the glass substrate, and the surrounding water medium were taken into consideration while solving for the electromagnetic field distribution.

To determine the force exerted on a particle, a virtual spherical surface which enclosed

the entire particle was necessary to calculate the electromagnetic field on this surface. In this work, we assume the particle is separated from waveguide surface by 60nm and 1W input power is launched as the initial condition. The waves were launched into these waveguides with the boundary mode, in other words, we do not take into account the contribution of the coupling loss. By using Maxwell stress tensor and integrating it over the surface enclosing particle, then we are able to obtain the optical forces exerting on a particle [17].

2-3-1. Waveguide geometry dependence of optical force

In order to investigating the dependence of optical force on waveguide geometry, we build the waveguide structures with different cross-sections here. Geometric parameters for the simulations used in our investigation are list in Table.2-1. The polystyrene particle with 1 and 2 μm in diameter dispersed in water can mimic most biological cells. We launch the transverse-electric (TE) polarized fundamental mode into each one to transport particles.

domain	material	Domain size	Refractive index
Waveguide	Silicon nitride	width(w) \times thickness(t)	2.2
		(w = 0.5, 1 and 2 μm , t = 200 and 300nm)	
Substrate	Silicon oxide	lower subdomain	1.45
cladding	Water	indefinite	1.33
particle	polystyrene	1 μm , 2 μm	1.59

Table.2-1. Simulation and geometric parameters

Fig.2-3 illustrates wavelength dependence of the propulsion force (F_x) for a 2 μm polystyrene sphere which is displaced at the horizontal center and separated from waveguide surface by 60nm. For each curve (waveguide of w = 0.5 μm and t = 200nm for example), the propulsion force first raises along with red-tuning the wavelength (region I) because the

evanescent field with longer wavelength extends deeper into water surrounding and interacts stronger with the particle. Then the force reaches a peak value when the interaction becomes the strongest. Furthermore, as the wavelength keeps red-tuning, the force drops gradually (region III), it is resulted from evanescent field extending beyond the particle and thus less evanescent field interacts with the particle. We use wavelengths λ of 1000nm, 1500nm and 2000nm to describe these profiles. Fig.2-4 shows the y component of electric field distribution at $y = y_{\text{particle center}}$ with the corresponding wavelengths.

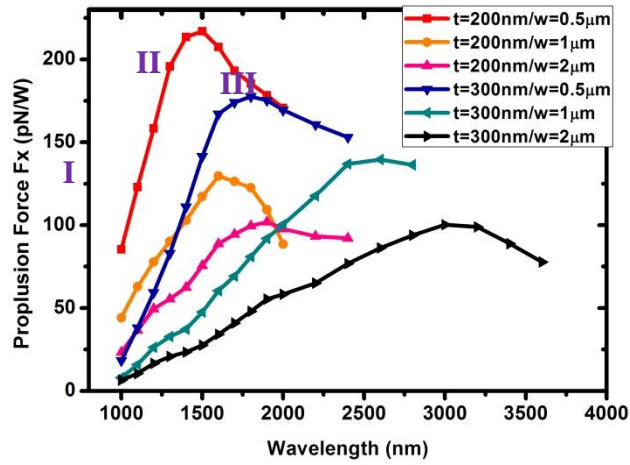


Fig.2-3. Wavelength-dependent propulsion force F_x for these geometries.

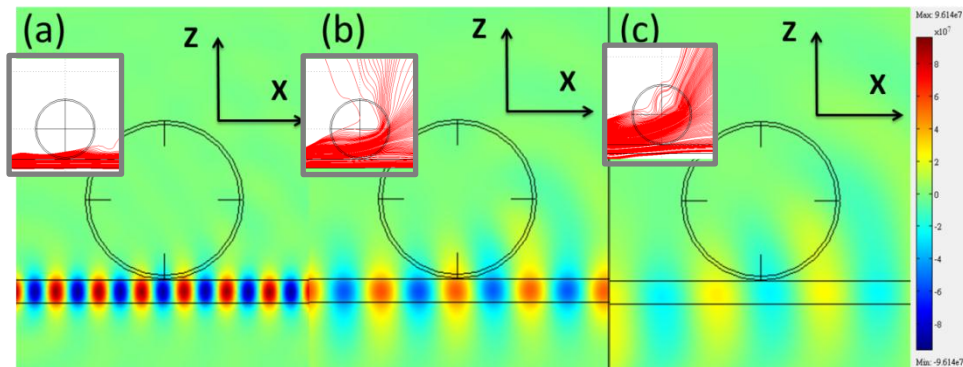


Fig.2-4. The distribution of y component of electric field at $y = y_{\text{particle center}}$ for (a) $\lambda = 1000\text{nm}$ (b) $\lambda = 1500\text{nm}$ (c) $\lambda = 2000\text{nm}$. Inset shows the streamline of power flow, respectively.

When launching wavelength is 1000nm, the y component of electric field distribution is more condensed in the waveguide than others. Thus the particle experiences less interaction with the evanescent field. For the condition with 2000nm launching wavelength, although the amplitude of the y component of electric field is relatively small, the extend part of evanescent field interacts sufficiently with the particle. The propulsion force became larger than the previous condition. However, the losses also increased because of the more scattered wave. Here the most suitable wavelength is about 1550nm. Its evanescent field can provide the greatest interaction with the trapped particle.

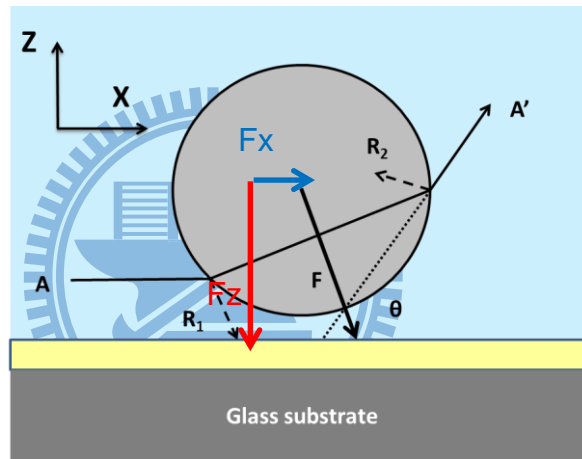


Fig.2-5. Diagram showing the ray optics of a spherical Mie particle trapped and propelled on the waveguide in water surrounding. The evanescent wave driven forces is separated by propulsion force and downward trapping force.

These profiles can also be explained by the momentum transfer in the system. The proposed model is shown in Fig.2-5. The principal part of the momentum transfer from incident light to the particle is due to the scattered rays which are refracted by the particle. The force exerted on a particle is given by the total change in the momentum of the incident photons. Because the momentum change of the ray from A to A', we get a combination force which consisted trapping and propulsion forces. It also shows that a larger scattered angle θ

will result in stronger propulsion component of optical force on the particle in x direction. Fig.2-5 also illustrates that the trapping force $-F_z$ will be greater than the propulsion force F_x .

The streamline of the power flow have been showed in the inset of Fig.2-4. It is obviously that the incident light wave is scattered by the particle with the largest scattered angle when the $\lambda=1500\text{nm}$ compared with other conditions, thus there is the strongest propulsion force.

Fig.2-3 also suggests that the thinner and narrower waveguide can reach stronger peak propulsion force at shorter wavelength. Base on this concept, we would be able to build an efficient transport system on a chip. For better coupling efficiency in experiments, we choose the thickness of 300nm instead of 200nm as our main parameter.

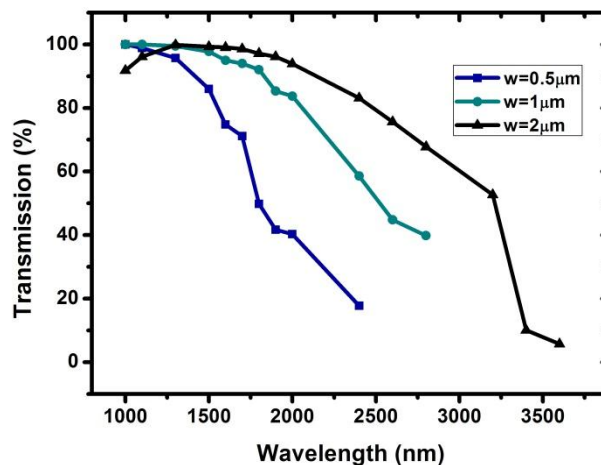


Fig.2-6. The diagram shows the wavelength-dependent transmissions for these waveguides in the single trapped particle system.

For the purpose of parallel manipulate, the guide wave must be strong enough to interact with other particles attracted subsequently after passing by one particle. We thus have to take into consideration that the transmission declines due to the existence of trapped

particle. We include this consideration by multiplying the propulsion force with transmission (T). The transmission is the percentage of guided power transmitted through waveguide section nearest to a single trapped particle. Fig.2-6 shows the transmission as functions of launching wavelength. It declines as red-tuning the launching wavelength.

The Fig.2-7 illustrates the propulsion force-transmission products as functions of launching wavelength. The high product guarantees that the waveguide will be able to transport a large amount of particles efficiently at the same time. Each peak wavelength is shorter than its counterpart in Fig.2-3. It means that we may sacrifice the propulsion force slightly for higher force-transmission product.

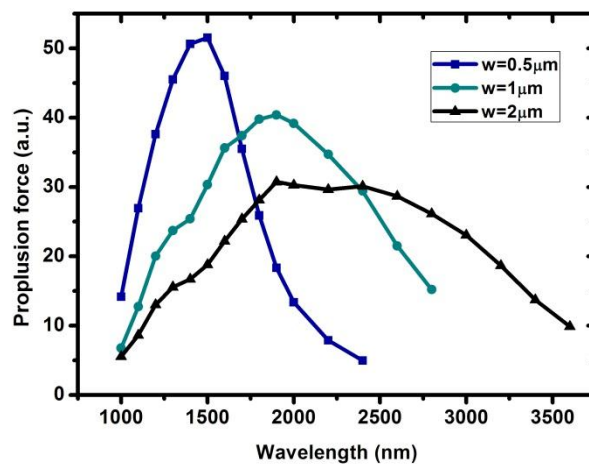


Fig.2-7. The products of propulsion force and transmission as functions of launching wavelength.

Similarly, we calculate the wavelength-dependent downward trapping forces F_z for these waveguides as shown in the Fig.2-8. The downward trapping force has a valley which represents the particle will be trapped most stably at the corresponding wavelength for each curve. It is worthy to note that, for each curve, the peak wavelength of the product almost coincides with the valley wavelength of the downward trapping forces. Hence we can

transport many particles simultaneously along the waveguide efficiently without easily disturbed when operated at the peak wavelength of force-transmission product.

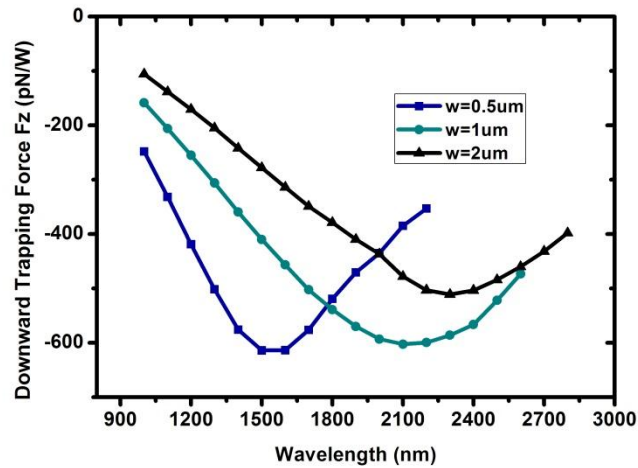


Fig.2-8. Calculation of the downward trapping forces F_z on different width of waveguides for a wide range of wavelength with 300nm thickness.

Among these waveguides, 0.5 μm wide waveguide is the most efficient and stable one. As we operate the launching wavelength which near 1500nm, the better downward trapping and propulsion forces exerting on the particle are 614 and 142 pN, respectively. At the same time, the forces are much stronger than what wider waveguides provide near 1500nm in wavelength. Here we also calculate the resultant of forces of gravity and buoyancy is 2.05×10^{-3} pN, and it is not at all affected for stable trapping.

2-3-2. Particle position dependence of optical forces

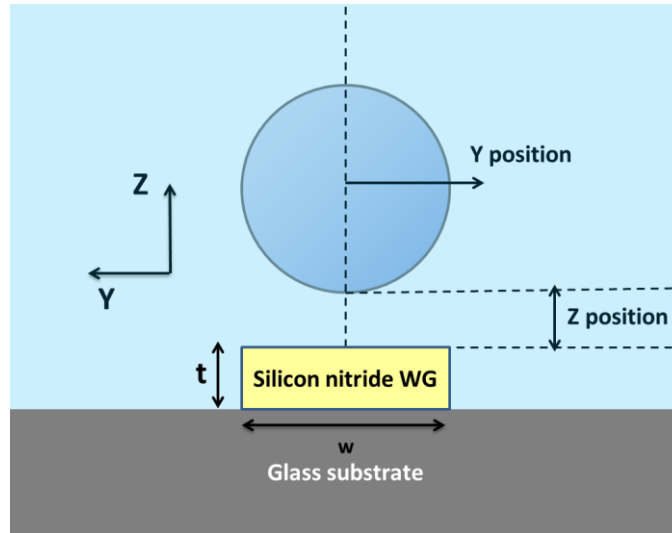


Fig.2-9. The diagram of cross-section of the system

To investigate stability of the trapped particle, we construct the system as shown in Fig.2-9. By the numerical calculation, we can detail the three-dimensional electromagnetic forces acting upon particle as functions of the position of particle at 1500nm and 1550nm in wavelength, which are upper and lower limits of the available wavelength in our measurement, respectively. From the force analysis, we were able to extract a parameter commonly used to describe optical traps: the trapping stiffness S which is defined as [18]

$$S \equiv \left(\frac{\partial F_i}{\partial x_i} \right)_{\text{equilibrium}} \quad m \quad (2-20)$$

it is the derivative of the restoring force with respect to the position of particle perturbed around the equilibrium point. We also note that the decay length (defined as the length where the force declines to e^{-1} times) for the force decreases in the z direction.

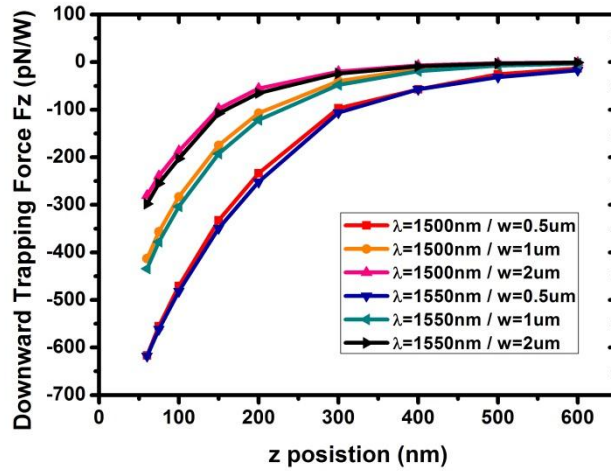


Fig.2-10. Comparison of the downward trapping forces F_z on a particle with $2\mu\text{m}$ in diameter using different waveguides and launching wavelengths (1500 and 1550 nm) at varying vertical positions.

$Z=60\text{nm}$	$\lambda=1500\text{nm}$			$\lambda=1550\text{nm}$		
Width(μm)	0.5	1	2	0.5	1	2
Z-axis stiffness ($\text{pN nm}^{-1}\text{W}^{-1}$)	4.1	3.8	2.7	3.8	3.7	2.9
Decay length(nm)	143	105	88	153	111	92

Table.2-2. The characteristic trapping stiffness and decay length of the force profiles in Z-direction.

We calculate the forces at different positions in the lateral directions (perpendicular to x direction). These values are computed for 1W. We first compute the downward trapping force along z direction (F_z) at horizontal center of the waveguide as shown in Fig.2-10. A feature we observe is that the maximum F_z of these waveguides located at the position nearest to the waveguide surface. F_z declines fast once the particle separates from the waveguide surface for a few hundreds of nanometer. The trapping stiffness and decay length of the force profiles are shown in Table.2-2. The trapping stiffness for the $0.5\mu\text{m}$ wide waveguide is an

order of magnitude higher than that of silicon waveguide [19] ($1.34\text{pN nm}^{-1} \text{W}^{-1}$ for 2000nm particle). And it is also larger than the stiffnesses for wider ($1\mu\text{m}$ and $2\mu\text{m}$) waveguides made of silicon nitride.

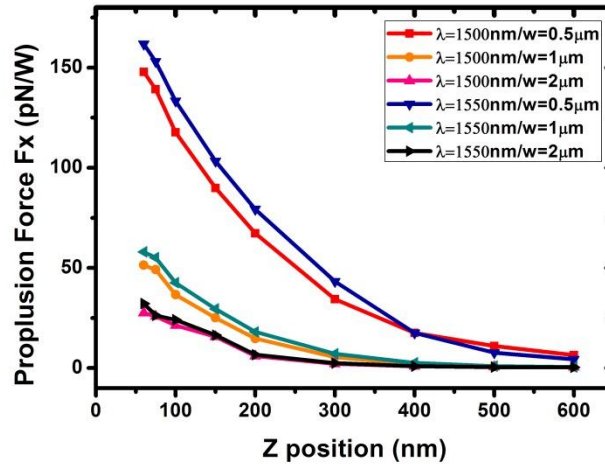


Fig.2-11. Comparison of the propulsion forces F_x at varying vertical positions.

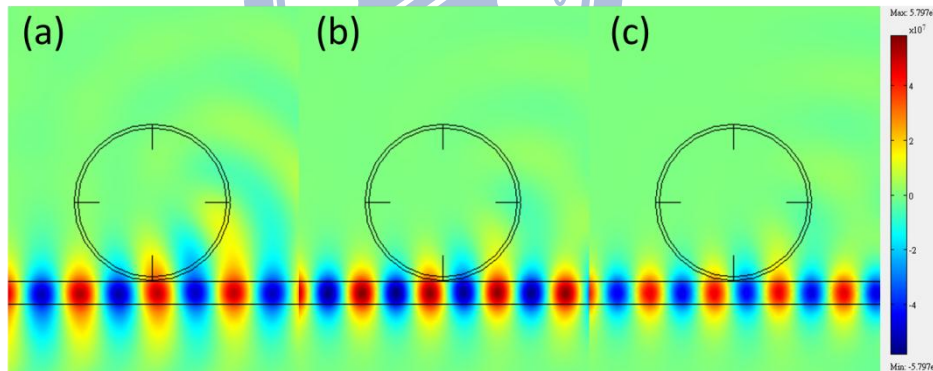


Fig.2-12. The distribution of y component of electric field at $y=y_{\text{particle center}}$ for (a) $0.5\mu\text{m}$ (b) $1\mu\text{m}$ (c) $2\mu\text{m}$ wide waveguides.

We can also get the propulsion force distributed along z direction at horizontal center of the waveguide as shown in Fig.2-11. It similarly depends on width. The narrower waveguide have larger propulsion force. This situation can be explained in Fig.2-12. When the wavelength is operated at 1500 nm, the narrower waveguide have the stronger evanescent

field extending into water surrounding. The 0.5 μm wide waveguide exhibited the highest stiffness and propulsion forces.

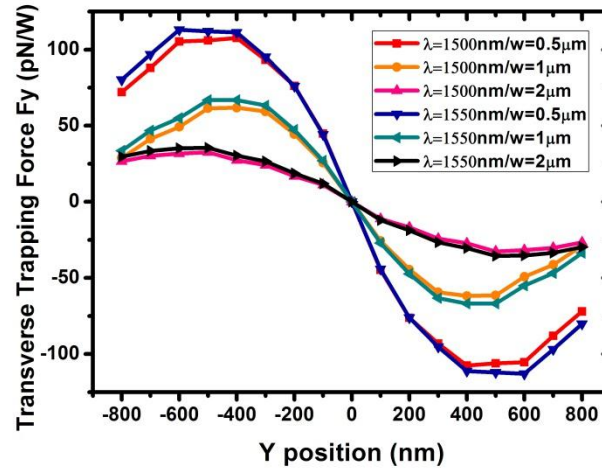


Fig.2-13. Comparison of the transverse trapping forces F_y on a particle with $2\mu\text{m}$ in diameter using different waveguide at $\lambda=1500$ and $\lambda=1550$ nm.

Fig.2-13 illustrates the surface transverse trapping force (F_y) as a function of y position when particle is 60nm above the waveguide surface. F_y is weaker at the horizontal center of the waveguide, and becomes stronger when the particle is near the edge of the waveguide. For the same particle size, the narrower waveguide exhibits stronger F_y . This is due to the discontinuity of electric field at the edge of the waveguide, which is necessary for maintaining the continuity of electric displacement.

Y=0nm	$\lambda=1500\text{nm}$			$\lambda=1550\text{nm}$		
Width(μm)	0.5	1	2	0.5	1	2
Y-axis Stiffness ($\text{pN nm}^{-1}\text{W}^{-1}$)	0.34	0.21	0.08	0.35	0.22	0.09

Table.2-3. The characteristic trapping stiffness of the force profiles in Y-axis

The characteristic trapping stiffness of the force profiles are shown in Table.2-3. The

transverse trapping stiffness for the 0.5 μm wide waveguide is higher than that of silicon waveguide (0.12pN nm⁻¹ W⁻¹ for 2000nm particle). And it is also larger than the stiffnesses for wider (1 μm and 2 μm) waveguides made of silicon nitride.

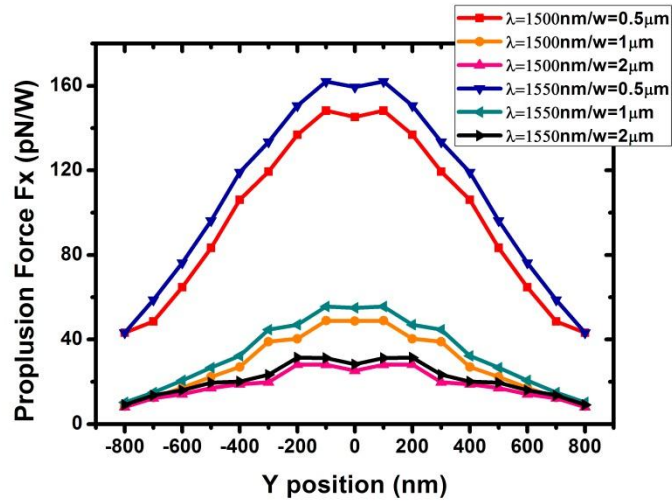


Fig.2-14. Comparison of the Propulsion forces Fx using different waveguide at $\lambda=1500$ and $\lambda=1550$ nm.

The dependence of propulsion force Fx on the position along y-axis is shown in Fig.2-14. It displayed the 0.5 μm wide waveguide can propel the particles with a wide range of transverse distance more efficient than the other waveguides.

2-3-3. Enhancement of optical forces by Indium Tin Oxide layer

In order to further improve the efficiency and the stability of particle manipulation, here we introduce an indium tin oxide layer between the waveguide and the glass substrate. The schematic is shown in Fig.2-15.

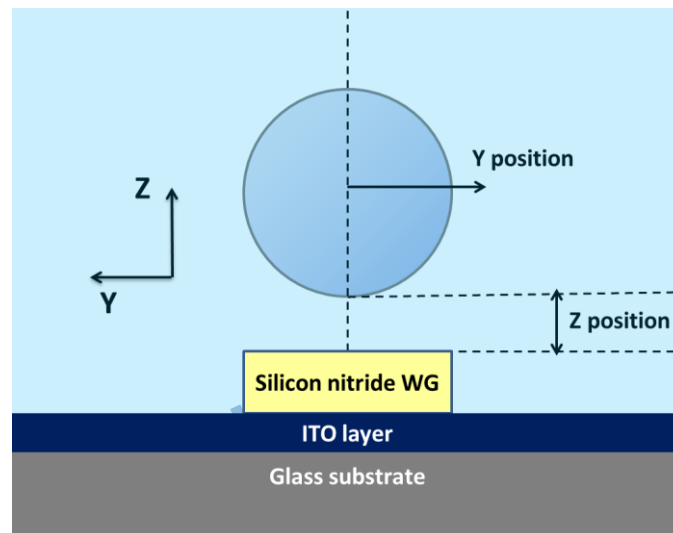


Fig.2-15. The cross-section of the system with the ITO layer.

Because of the conductor-like optical property of ITO layer with complex dielectric function ($\epsilon_r = -2 - 0.5i$ near 1500nm in wavelength [20]), the guide mode will be forbidden extending into ITO film, and thus it distributes asymmetric in z direction with stronger evanescent field extending into water surrounding as shown in Fig.2-16(d) (with ITO film) compared to Fig.2-16(e) (without ITO film). A thicker ITO layer can force the guided mode to extend deeper into the upper surrounding as shown from Fig.2-16(d) to (a). The resulting optical force (F_x for example) upon $2 \mu\text{m}$ particle on $0.5 \mu\text{m}$ wide waveguide as a function of the thickness of ITO layer is shown in Fig.2-16.

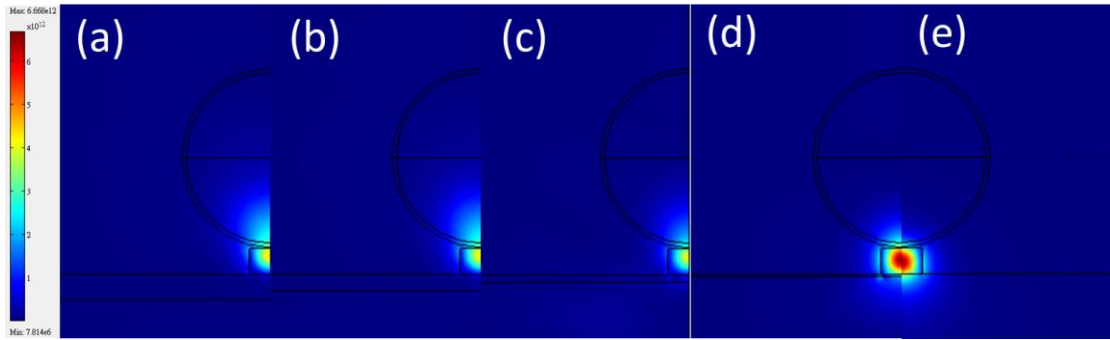


Fig.2-16. Comparison of guided power distributions on 0.5 μm wide waveguide for (a) 300 nm (b) 200 nm (c) 100 nm (d) 30 nm (e) none thicknesses of ITO layer.

The indium tin oxide layer is conductor-like film, so the electromagnetic field is affected by the boundary condition of the conductor. It also involves surface plasmon polariton which is the coherent electron oscillations that exist at the interface between metal and dielectric materials. Fig.2-17 shows the interaction of free electrons on metal surface and the electromagnetic field, we can see that the surface plasmon polariton is the TM wave only upon the metal surface which is caused by the tangent of electric field must be continuous. However, the fundamental mode of the used waveguide is the TE-like mode, there is no field distribution within the metal and at the interface between metal and dielectric materials, and hence the mode will be propelled upward.

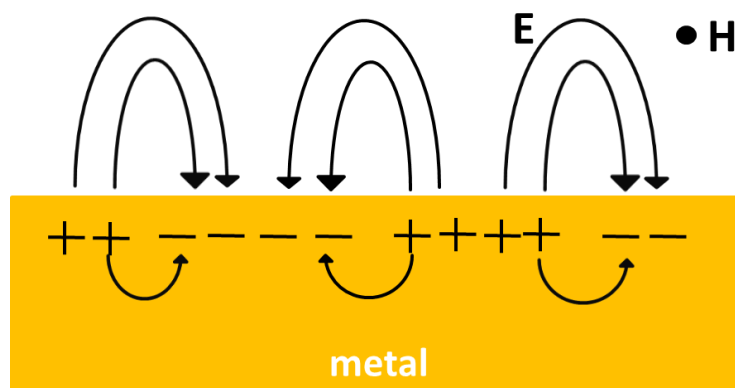


Fig.2-17. The scheme of the electromagnetic field distribution of surface plasmon polariton at the interface between metal and dielectric materials.

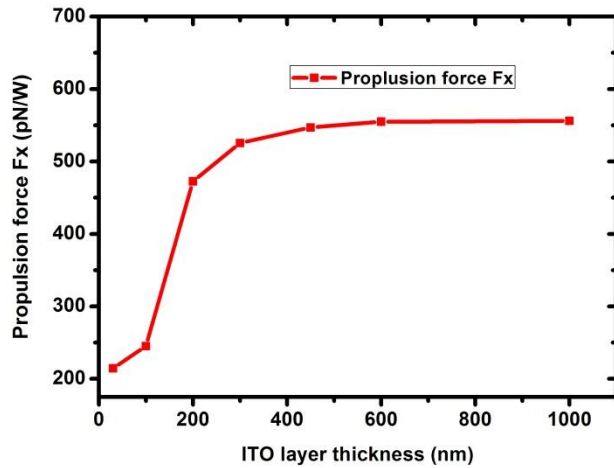


Fig.2-17. The dependence of ITO layer thickness propulsion force F_x for $0.5 \mu\text{m}$ wide waveguide. (Operated at 1550nm)

In order to achieve better propulsion forces in experiments, we have to choose a feasible thickness to increase the interaction between particles and evanescent field. We see that the value increased rapidly as the thickness reached 200nm , and then the propulsion force became saturated. Due to that the customized ITO substrate we already have is 200nm thick in the ITO layer, the following simulation investigating the merits of using ITO are conducted with 200nm thick ITO layer. In this condition, it still has a great enhanced propulsion force.

Similarly, we compute the downward trapping force F_z as the particle position varied along z axis at the horizontal center above the waveguide with 200nm ITO layer as shown in Fig.2-17. Compared with F_z on particle above the waveguide without ITO layer (Fig.2-8), the ITO layer does enhance F_z significantly.

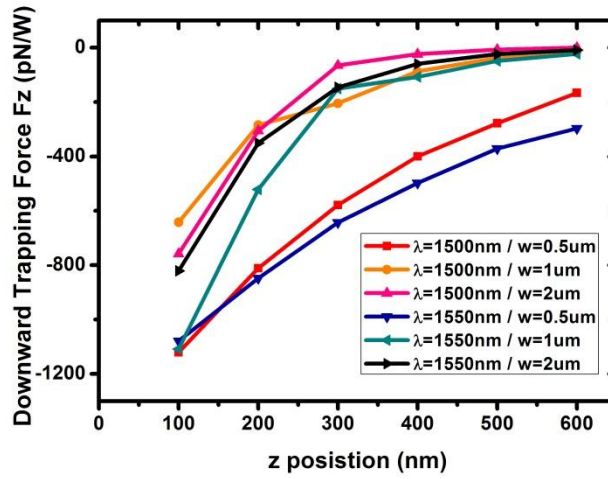


Fig.2-18. ITO layer enhanced downward trapping force F_z at varying vertical positions.

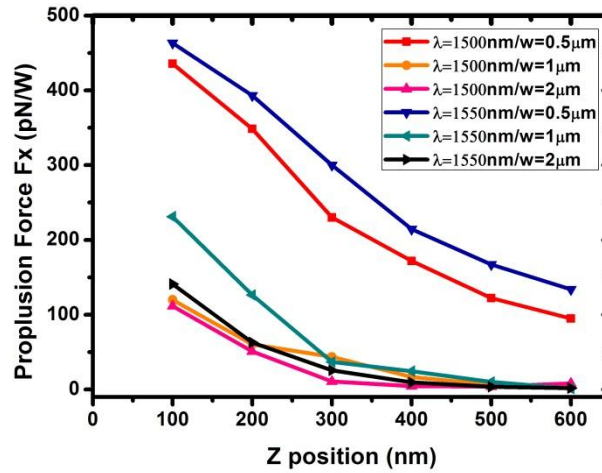


Fig.2-19. ITO layer enhanced propulsion force F_x at varying vertical positions.

Here we emphasize the enhancement of propulsion force which is associated with the particle velocity in experiments. Fig.2-19 shows the substantial increments of the propulsion force. Notably, the $0.5\ \mu\text{m}$ wide waveguide exhibit the more excellent propulsion forces than others. The calculated optical force in y direction (F_y) is shown in Fig.2-20. The transverse trapping ability described by Y-axis stiffness is shown in Table.2-4. The $0.5\ \mu\text{m}$ wide waveguide also have the highest stiffness in transverse direction by enhanced optical force.

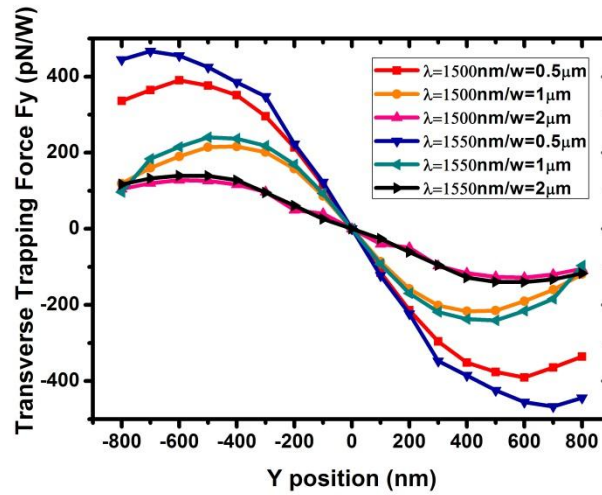


Fig.2-20. ITO layer enhanced transverse trapping force F_y at varying transverse positions.

Y=0nm	$\lambda=1500\text{nm}$			$\lambda=1550\text{nm}$		
Width(μm)	0.5	1	2	0.5	1	2
Y-axis Stiffness ($\text{pN nm}^{-1}\text{W}^{-1}$)	1.02	0.72	0.30	1.15	0.78	0.31

Table.2-4. The characteristic trapping stiffness of the force profiles in Y-axis

Although the conductor-like property of ITO layer also causes additional propagation loss, the ability to further enhance optical forces is still beneficial for short distance transportation on a chip.

Finally, we use $0.5\mu\text{m}$ wide waveguide as example to show the enhancement caused by ITO layer. Compared the effects with and without the existence of the 200nm thick ITO layer, we summarized the force in three dimensions in Fig.2-21. The particle all moved from the equilibrium point. It is obvious that the forces are enhanced by ITO layer, and then the particles would be trapped more stably. The characteristic trapping stiffness and maximum forces of these force profiles are shown in Table.2-5. We observe that the Y-axis stiffness and the forces almost increase by at least 2 times enhancement. Especially, the propulsion forces

are enhanced by almost 3 times. It indicates the waveguide with ITO layer underlaid can manipulate particles more efficiently.

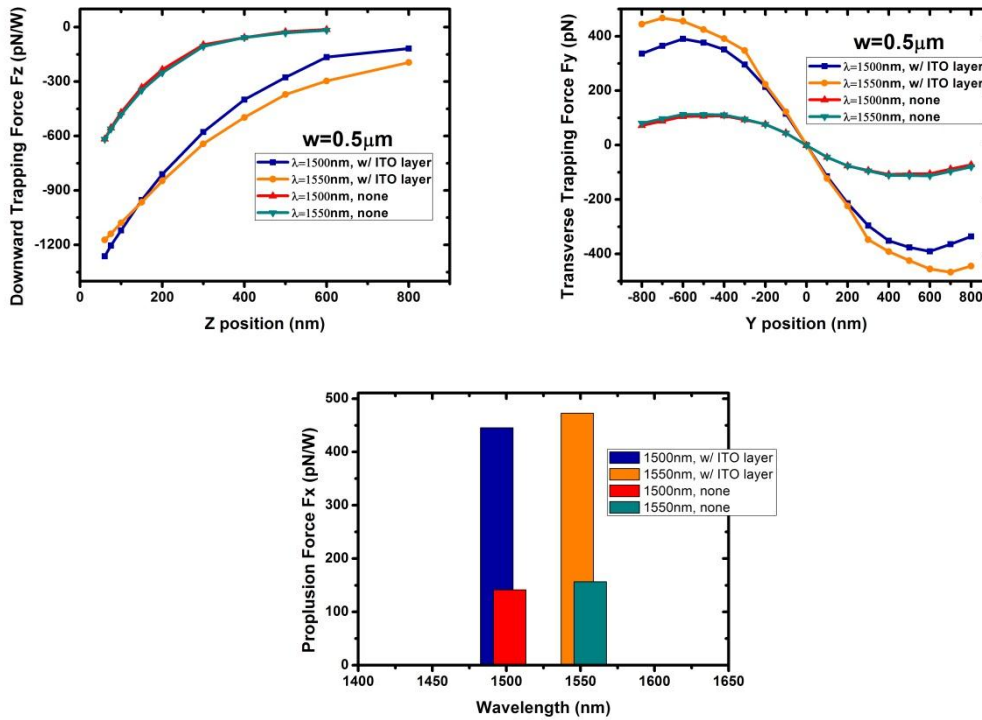


Fig.2-21. Comparison of the forces for 0.5 μm wide waveguide with ITO layer or not in three dimensions.

	1500nm		1550nm	
	w/o	w/	w/o	w/
Z-axis S ($\text{pNnm}^{-1}\text{W}^{-1}$)	3.9	3.8	4.1	2.2
Max Fz (pN/W)	617	1262	618	1173
Decay length(nm) in Z	143	310	153	396
Y-axis S ($\text{pNnm}^{-1}\text{W}^{-1}$)	0.34	1.02	0.35	1.15
Max Fx (pN/W)	142	445	156	473

Table.2-5. The characteristic trapping stiffness and maximum forces of the force profiles

2-4. Summary

In this section, when operating at the peak wavelength of force-transmission product, the waveguide will provide efficient and stable parallel-transport of micro-sized particles. We also observe that these waveguides with ITO layer underlaid can attract and propel the particles with improved downward trapping force and propulsion force, respectively. These forces further exceed what waveguides without ITO layer can provide. Among these waveguides, 0.5 μm wide waveguide with ITO layer is the most efficient and stable one in this analysis. Especially, it has three times enhancement of propulsion force compared with the counterpart without ITO layer.



Chapter 3.

Fabrication and measurement

3-1 Fabrication

The waveguides are made of ITO glass substrate covered by silicon nitride strips. The ITO layer is 200nm in thickness. Our waveguide structures are fabricated from silicon nitride film. At first, silicon nitride film is deposited on the ITO glass substrate by using plasma-enhanced chemical vapor deposition (PECVD). The film thickness is 300nm. Then a 240 nm polymethylmethacrylate (PMMA) layer is spun on the sample by a spin coater. The strip pattern is defined on the PMMA layer by using electron beam lithography (EBL) with three different widths ($w = 0.5, 1, \text{ and } 2\mu\text{m}$). The first process flow is illustrated in Fig. 3-1.

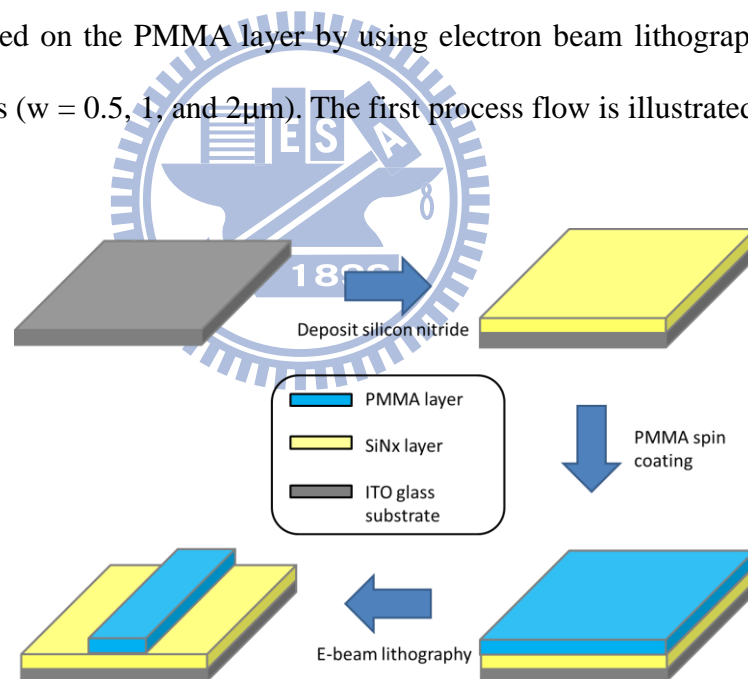


Fig.3-1. The first part of fabrication process

Then the pattern defined on PMMA is transferred to silicon nitride layer by using reactive ion etching (RIE). The residual PMMA layer can be removed by O_2 plasma. The second process flow is illustrated in Fig. 3-2. The SEM image of finished optical silicon nitride waveguide structures after these steps are shown in Fig.3-3.

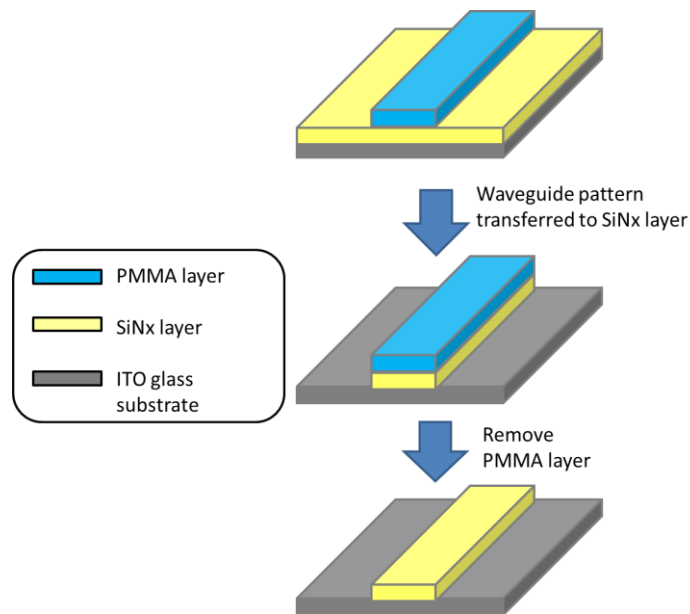


Fig.3-2. The second part of fabrication process

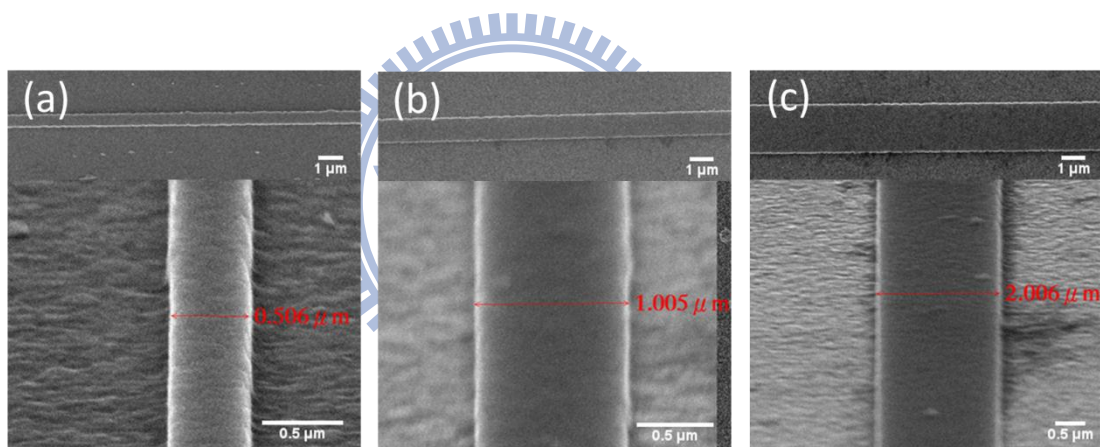


Fig.3-3. The top- and tilted-view SEM pictures of these structures (a) $w=0.5\mu\text{m}$ (b) $w=1\mu\text{m}$ (c) $w=2\mu\text{m}$

Because the patterns are defined by EBL in the $600\times 600\mu\text{m}^2$ field size, the total length of each waveguides is limited around $550\mu\text{m}$. It is necessary to make an entrance for coupling light at one end of the waveguide. Generally, we used to cleave the substrate to complete this step, but there are a lot of difficulties for cleaving the glass substrate because there is no crystallographic orientation on it, and it is too hard to be cleaved. So we use the process of mechanical polishing to make a waveguide entrance for light coupling. After the waveguide

structures are defined on silicon nitride layer, the process of mechanical polishing has two steps. The polishing reagent is water. The cross-section of waveguide entrance is shown in Fig.3-4.

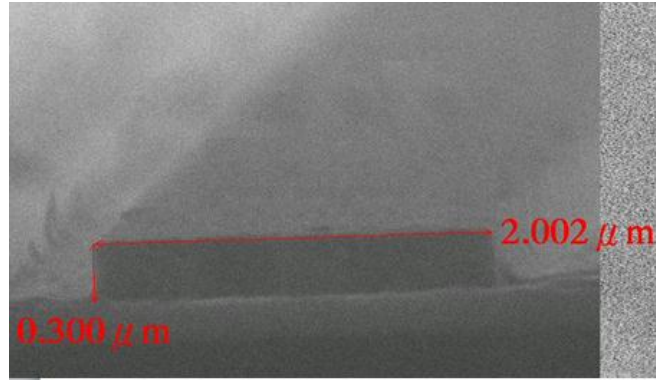
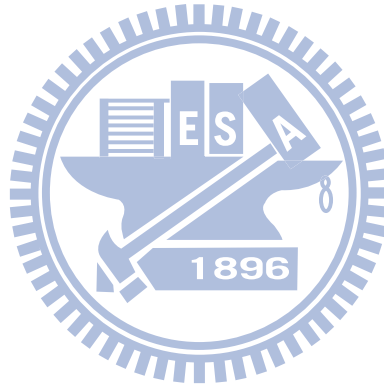


Fig.3-4. The cross-section of entrance of 2μm wide waveguide.



3-2. Measurement setup

The measurement setup is schematically illustrated in Fig. 3-5. A cell made up of ~0.11 mm thick double-sided tape and a cover slip is glue on the sample surface for forming a chamber, which contains the particles dispersed in de-ionized water. Thus the waveguides are covered by water surrounding. We use polystyrene micro-spheres (with 1 and 2 μm in diameter, $n = 1.59$) with standard deviation smaller than 1% suspended in de-ionized water and add 1%-by-volume Triton X-100 non-ionic surfactant to the particle solution to prevent aggregation of the nanoparticles and to minimize adhesion between micro-particles and the surface of the devices.

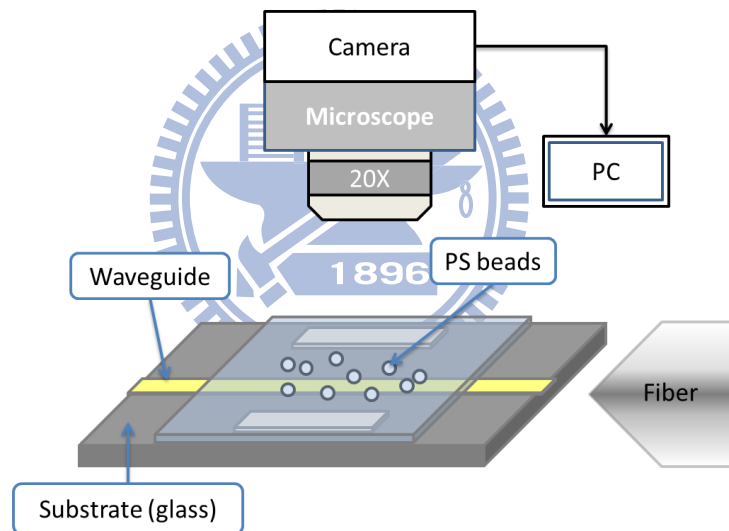


Fig.3-5. The diagram of the experimental setup

The continuous laser source is given by HP 8168 tunable laser with erbium doped fiber amplifier, and it operates at the range from 1480nm to 1580nm. The fiber is mounted on micro-positioning stages. Light is injected into the waveguides through a fiber with tapered tip, which is directly immersed in water. We use continuous laser source with 1500nm and 1550nm in wavelength to do the measurements. The output powers of 1500nm and 1550nm at the tapered end of fiber are 57mW and 55.6mW, respectively.

The measurement setup is shown in Fig. 3-6. An optical microscope with illumination from above and a microscopic objective lens with 20 times magnification were used to observe the motion of particles. A CCD camera was mounted on top of the microscope and the images were captured on a computer.

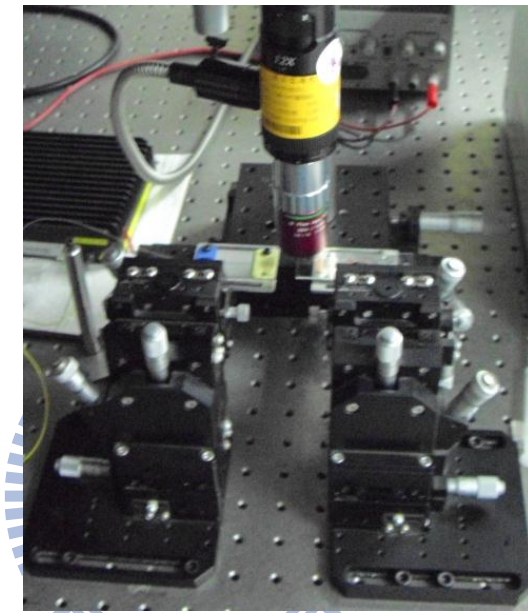


Fig.3-6. The experimental setup

3-3. Measurements and discussion

3-3-1. Particle transportation velocity

All particle transportation velocities are measured at 100 μm away from the input ports of the waveguide. Fig.3-7 (a)-(c) shows the $2\mu\text{m}$ particles move as time evolves on 0.5, 1, and $2\mu\text{m}$ wide waveguides, respectively, when the continuous-wave laser source operated at 1500nm. Fig (d)-(f) shows the same system under condition of 1550 nm in wavelength.

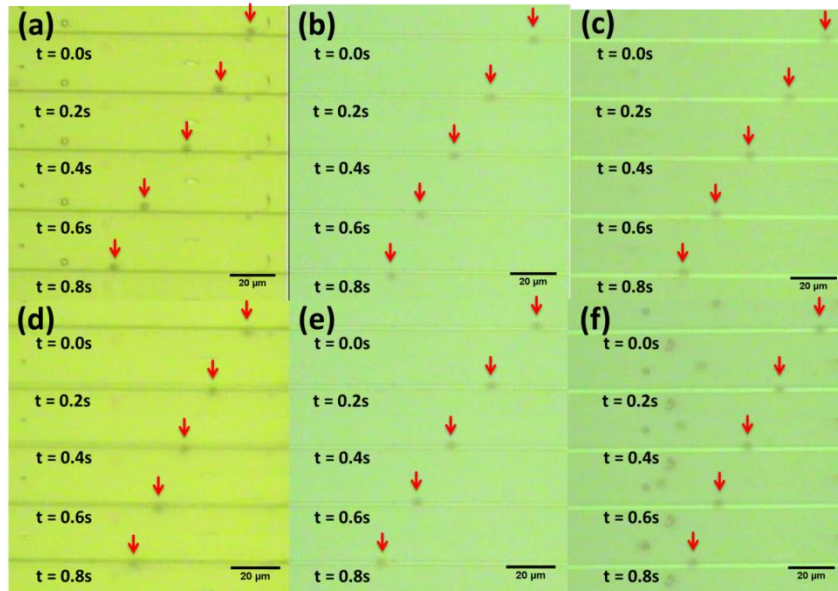


Fig.3-7. Motion of $2\mu\text{m}$ particles (indicated by red arrows) as time evolves on (a) 0.5, (b) 1, and (c) $2\mu\text{m}$ wide waveguides in 1500nm waveguide. (d) (e) (f) shows the same system which under condition of 1550 nm in wavelength.

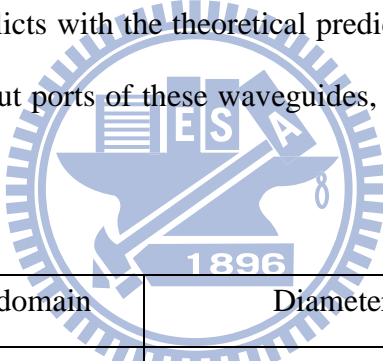
We average the velocities among more than five samples for each experiment. In order to understand the contribution of optical force by optical waveguides, we measured the velocity without any structure on the substrate as the background velocity (V_b) caused by the wave scattered from the fiber tip. The background velocity is about $37\mu\text{m/s}$ for $2\mu\text{m}$

polystyrene particles. The average velocity (V_{av}) and the difference ($V_{ab}-V_b$) between average velocity and background velocity are shown in Table.3-1.

$\lambda=1500nm$			$\lambda=1550nm$		
width (μm)	V_{av} ($\mu m/s$)	$V_{av} - V_b$ ($\mu m/s$)	width (μm)	V_{av} ($\mu m/s$)	$V_{av} - V_b$ ($\mu m/s$)
0.5	70	33	0.5	60	23
1	78	41	1	79	42
2	75	38	2	70	33

Table.3-1. The measured velocities of 2 μm particles

We noticed that the relation between waveguide width and the measured particle transport velocity itself conflicts with the theoretical prediction. Because there is no coupling structure designed at the input ports of these waveguides, the power ratios coupled into each waveguide are different.



domain	Diameter
Cladding	125 μm
Fiber core	8 μm
Tip	2 μm (radius of curvature)

Table.3-2. Simulation and geometric parameters of taper fiber.

In order to estimate the coupling efficiency, we construct a three-dimensional coupling model in FEM simulation which consists of a fiber tapered by 30° at the tip, as manufacturer specified, and a waveguide structure on glass substrate. The distance between the fiber tip and waveguide is assumed to be 3 μm . The geometric parameters of the single mode taper fiber specified by the manufacturer are list in Table.3-2. In order to prevent the simulation out of the computational memory, here we did not introduce the 200nm ITO layer between the

waveguide and substrate. The efficiencies are estimated to be 0.006, 0.012, and 0.028 for the cases of 0.5, 1, and 2µm wide waveguides, respectively.

For fair comparison, we normalize the velocities by the estimated powers coupled into the waveguides. Here we used the wavelength at 1500nm for instance. The 2µm particle transport velocities when per watt power coupled into 0.5, 1, and 2µm wide waveguides are shown in Table.3-3.

width (µm)	$V_{av} - V_b$ (cm/s/W)
0.5	9.65
1	5.99
2	2.38

Table.3-3. The 2µm particle transport velocities when per watt power coupled into waveguides

The theoretical velocities are calculated by eqs. (2-15) is 1.2cm/s, 0.32cm/s, and 0.29cm/s, respectively. These differences may result from three causes. First, the existence of ITO layer fundamentally affects the boundary mode in simulations. Second, the distance between the waveguide and the fiber is variable in each experiment. And finally, there may be some deviations between the approximated hydrodynamic model and the practical waveguide system. Although the measured velocities are faster than those predicted theoretically, the result coincides with the predicted relation that a narrower waveguide can transport particles more efficiently.

Fig.3-8 shows the 1µm particles move as time evolves on 0.5, 1, and 2µm wide waveguides, respectively, with launching wavelength at 1500nm and 1550nm. The 1µm particles average velocity (V_{av}) and the difference ($V_{ab} - V_b$) between average velocity and

background velocity are listed in Table.3-4. In many observations, we find $1\mu\text{m}$ particles is easier to be disturbed than $2\mu\text{m}$ particles, because the size-dependent downward trapping force becomes weaker. It is obvious that the $1\mu\text{m}$ particles has velocities much slower than $2\mu\text{m}$ particles. This is because the evanescent field and the particle cannot interact significantly. Thus the transported velocity of $1\mu\text{m}$ particles degrades severely. It is almost that the wave directly scattered from the fiber tip transports the $1\mu\text{m}$ particles. Therefore, the difference ($V_{\text{ab}}-V_{\text{b}}$) between average velocity and background velocity may close to zero or even smaller than zero.

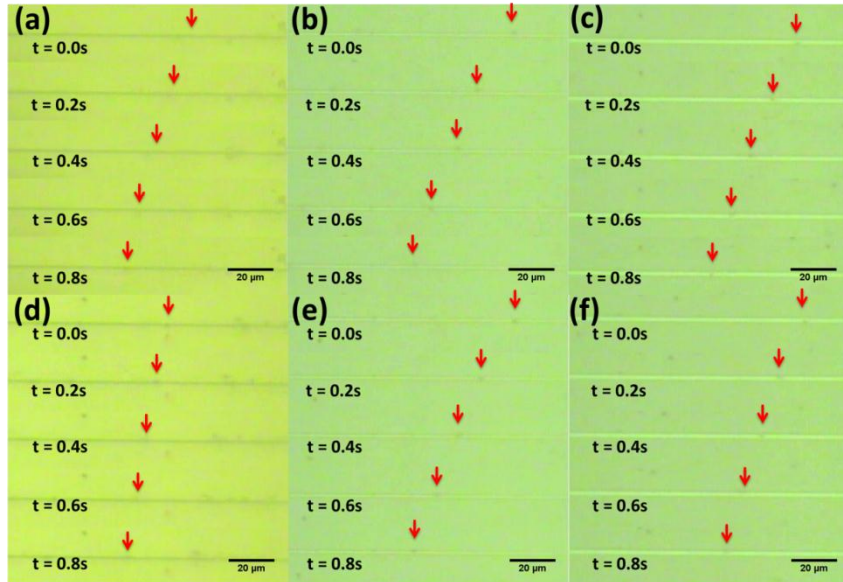


Fig.3-8. Motion of $1\mu\text{m}$ particles (indicated by red arrows) as time evolves on (a) 0.5, (b)1, and (c) $2\mu\text{m}$ wide waveguides in 1500nm waveguide. (d) (e) (f) shows the same system which under condition of 1550 nm in wavelength.

$\lambda=1500\text{nm}$			$\lambda=1550\text{nm}$		
width (μm)	V_{av} ($\mu\text{m/s}$)	$V_{\text{av}} - V_{\text{b}}$ ($\mu\text{m/s}$)	width (μm)	V_{av} ($\mu\text{m/s}$)	$V_{\text{av}} - V_{\text{b}}$ ($\mu\text{m/s}$)
0.5	30	3	0.5	23	-4
1	56	29	1	51	24
2	48	21	2	44	17

Table.3-4. The measured velocities of $1\mu\text{m}$ particles.

3-3-2. Sorting application

Here we mix $2\mu\text{m}$ with $1\mu\text{m}$ particles in water surrounding. The motions of particles are shown in Fig. 3-9. Due to that the optical forces depends on the size of particle, the mixed particles are separated by the difference of transporting velocity on the waveguide. Moreover, due to the weaker trapping force, the $1\mu\text{m}$ particle flow away from the waveguide and slow down after a few tens of micrometers. This function can be used to classify the particles by their size.

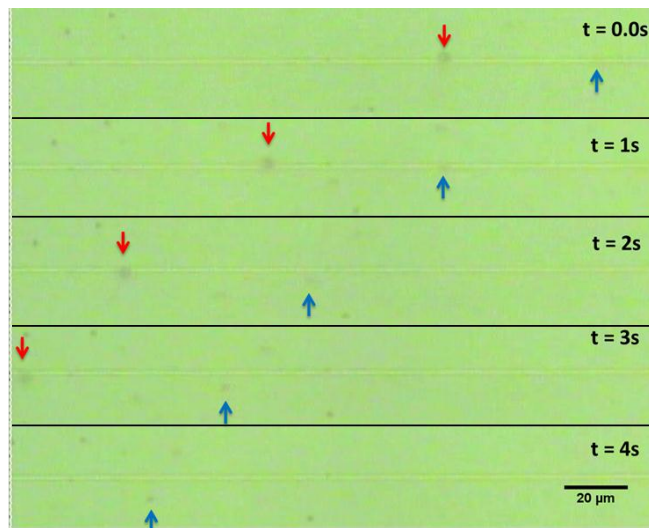


Fig.3-9. Motion of mix of $1\mu\text{m}$ and $2\mu\text{m}$ particles (indicated by red and blue arrows) as time evolves $1\mu\text{m}$ wide waveguides in 1500nm waveguide.

3-4. Summary

Due to the enhancement caused by ITO layer, our waveguide under a lower input power can transport particles much faster than that done by waveguide of the same width on silica film (as compared in [11]). With properly designed coupling structure, silicon nitride waveguide on ITO layer would be potential for developing efficient transport system on integration chip. Moreover, the propulsion efficiency of different size particles on silicon nitride waveguides open the way to sorting application, the classification of mixed particles by the size can be realized.



Chapter 4.

Conclusion and Future work

4-1. Conclusion

In this report, we attempt to construct an efficient particle transportation system by an easily coupled waveguide structure. The simple geometry of solid-core photonic waveguide is more suitable for easy-coupling than slot waveguides. Among various materials, silicon nitride waveguide with moderate refractive index had been proposed to yield stronger interaction, between particles and the evanescent field, than waveguides with higher or lower refractive index can do. How to improve the efficiency and stability of particle transportation on silicon nitride waveguide is what we devote to do. We have found that the narrower waveguide can reach stronger peak propulsion force at shorter wavelength. We investigate this relation by FEM simulation suggest that for parallel manipulation of particle transportation, a factor more important than propulsion force itself is the force-transmission product. Simulation results show that peak value of force-transmission product just coincides with the maximum downward trapping force in wavelength, where many particles could be transported simultaneously without easily disturbed. The better Y and Z-axis stiffness of 0.5 μm wide waveguide, compared with wider waveguides, also emphasize that a narrower waveguide can transport particles more stably.

For further improve the efficiency and stability of particle transportation, we introduce an ITO layer beneath the waveguide, which can forces guided wave to extend upward deeper into the water surrounding and enhance the interaction between particle and the evanescent field. The simulation results show that the ITO film do largely enhance the propulsion force

and trapping forces. Although the conductor like property of ITO film will induce additional propagation loss, the better transporting efficiency and stability still attractive for short-term particle transportation on integration chip. We fabricate the waveguide structures on ITO glass and measure the velocity of particle transportation. At 1500nm wavelength, the 0.5 μm wide waveguide with ITO layer underlaid can transport 2 μm particle with velocity of 9.65cm/s/W, which is much faster, as simulation predicted, compared with silicon nitride waveguides with the same geometric parameters without ITO film beneath. We also show that the waveguide we proposed is able to serve sorting application.



4-2. Future work

In our present works, the coupling configuration between input fiber and the waveguide is not efficient. Most power are scattered from the fiber tip but not coupled into the waveguide. Therefore the particles are not solely propelled by the guided wave. For solving this problem we have to include a coupling design at the waveguide entrance. We regarded grating coupler as a potential candidate for two reasons [21]. First, the fiber and waveguide are aligned nearly perpendicular to each other. This would eliminate the influences caused by the waves scattered directly from the input fiber. Second, there is no need to cleave the sample for coupling, which enables wafer scale testing and increases the amount of available devices on the sample. The grating coupler is shown in Fig.4-1.

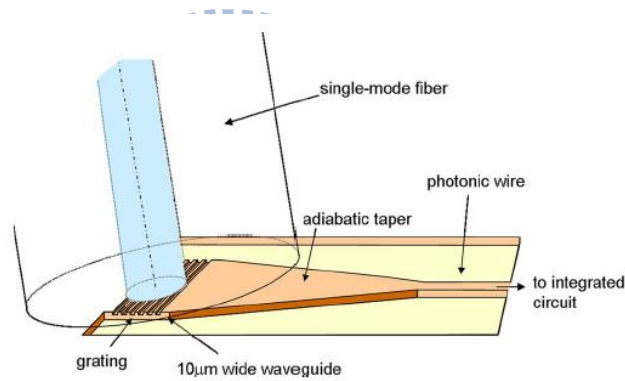


Fig.4-1. Coupling principle between fiber and photonic wires by means of a grating.

Except the coupling problem, we also attempt to transport real biological cells and integrate the waveguides with other devices into a chip for developing lab-on-chip system. Moreover, we can use the microfluidic system [22] to sort the different size particles. As the particles flow through the region of waveguide, the size-dependence of the optical force causes larger particles to be guided into a separated flow channel in Fig.4-2(a). Fig.4-2(b) shows that the parallel waveguides with different trapping abilities will transport the different size particles respectively.

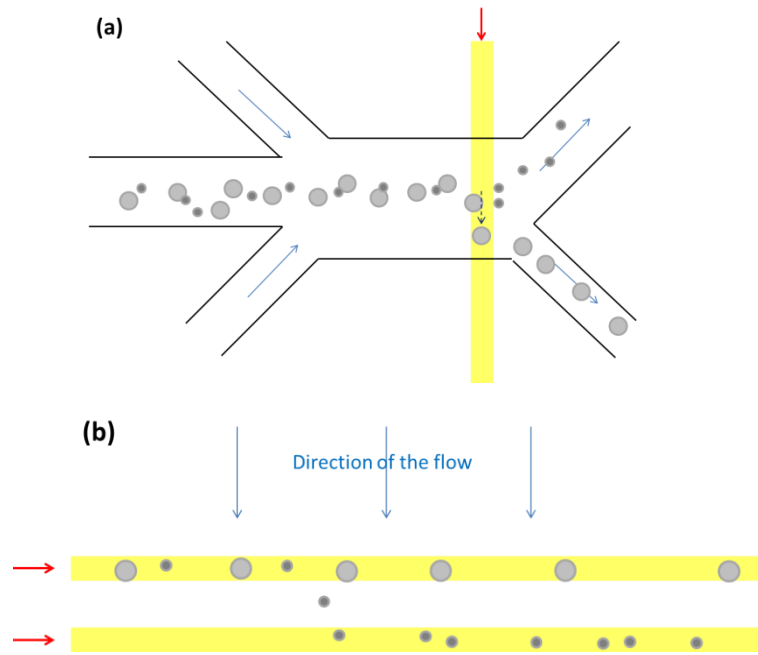
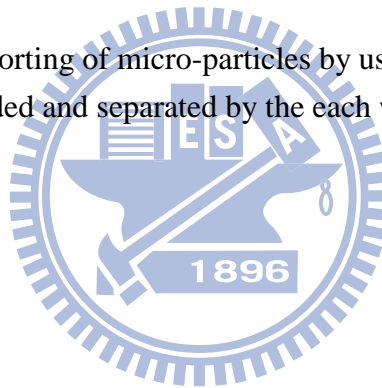


Fig.4-2. (a) Passive optical sorting of micro-particles by using the suggested waveguide. (b) The particles will be guided and separated by the each waveguide which have different trapping abilities.



Ch1.

- [1] A.L.Schawlow and C.H. Townes, Phys. Rev. Lett. **112**, 1940 (1958)
- [2] T.H. Maiman, Nature **187**, 493 (1960)
- [3] M. Yoshikawa, K. Shinohara, and R. Ueda, Appl. Phys. Lett. **31**, 699 (1977)
- [4] A. Ashkin, Phys. Rev. **24**, 156 (1970).
- [5] A. Ashkin, J.M. Dziedzic, J.E. Bjorkholm and S Chu, Opt. Lett. **11**, 288(1986).
- [6] S.kawata and T. Sugiura, Opt. Lett. **17**, 772 (1992)
- [7]P. C. Chaumet, A. Rahmani, and M. Nieto-Vesperinas, Phys. Rev. Lett. **88**, 123601 (2002).
- [8] K. Okamoto and S. Kawata, Phys. Rev. Lett **83**, 22 (1999)
- [9] M. Barth and O. Benson, Appl. Phys. Lett. **89**, 253114 (2006)
- [10] S. Kawata and T. Tani Opt. Lett. **21**,1768 (1996)
- [11] S. Gaugiran, S. Gétin, G. Colas, A. Fuchs, F. Chatelain, J. Dérourard, and J. M. Fedeli, *Opt. Express*, **13**, 6956(2005).
- [12] K. Grujic, O. G. Hellesø, J. S. Wilkinson, and J. P. Hole, *Opt. Commun.*, **239**, 227(2004).
- [13] A. H. J. Yang, S. D. Moore, B. S. Schmidt, M. Klug, M. Lipson and D. Erickson, Nature **457**, 71 (2009).

Ch2

- [14] J.P. Barton, D.R. Alexander, S.A. Schaub, J. Appl. Phys. **66**, 4594 (1989)
- [15] M. Born and E. Wolf, Principle of Optics (Pergamon, Oxford, 1993), 6th ed., p.633.
- [16] J.Y. Walz Appl.Opt. **38**, 5319(1999)
- [17] M. Nieto-vesperinas, P. C. Chaumet, and A. Rahamni, Phil. Trans. R. Soc. Lond. A **362**, 719 (2004)
- [18] Svoboda K and Block S M 1994 Annu. Rev. Biophys. Biomed. **23**, 247

[19] A.H. J. Yang and D. Erickson, *Nanotechnology*, **19**, 045704 (2008)

[20] G. Xu, Y. Chen, M. Tazawa, and P. Jin, *Appl. Phys. Lett.* **88**, 043114 (2006)

Ch.4

[21] F. V. Laere, M. Ayre, D. V. Thourhout, *Jourall of Lightwave Technology*, **25**, 1 (2007)

[22] R. F. Marchington, M. Mazilu, S. Kuriakose, V. Garcés-Chávez, P. J. Reece, T. F.

Krauss, M. Gu, and K. Dholakia, *Opt. Express*, **16**, 3712(2008).

